Atmospheric Environment 220 (2020) 117030

Contents lists available at ScienceDirect

Atmospheric Environment

journal homepage: http://www.elsevier.com/locate/atmosenv

Characterization of particulate matter emitted by a marine engine operated with liquefied natural gas and diesel fuels

Joel C. Corbin [a,*], Weihan Peng [b], Jiacheng Yang [b], David E. Sommer [d], Una Trivanovic [d], Patrick Kirchen [d], J. Wayne Miller [b,c], Steven Rogak [d], David R. Cocker [b,c], Gregory J. Smallwood [a], Prem Lobo [a], Stéphanie Gagné [a,**]

[a] Metrology Research Centre, National Research Council Canada, 1200 Montreal Road, Ottawa, Ontario, K1A 0R6, Canada
[b] Center for Environmental Research & Technology, University of California Riverside, 1084 Columbia Ave, Riverside, 92507, CA, USA
[c] Chemical and Environmental Engineering, University of California Riverside, 1084 Columbia Ave, Riverside, 92507, CA, USA
[d] Department of Mechanical Engineering, University of British Columbia, 2054-6250 Applied Science Lane, Vancouver, BC, V6T 1Z4, Canada

HIGHLIGHTS

- Detailed characterization of PM emissions from natural-gas-powered marine vessel.
- PM was primarily volatile organics, which may originate from lubrication oil.
- BC emissions were 37x higher when switching from liquid natural gas to diesel fuel.

GRAPHICAL ABSTRACT

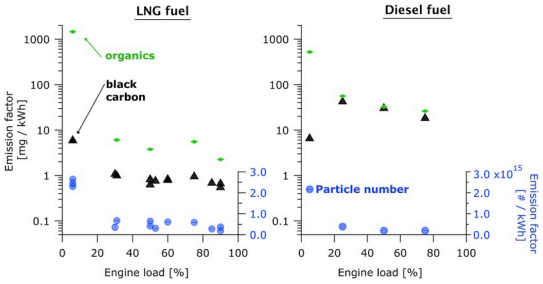

ARTICLE INFO

Keywords:
LNG
Natural gas
Marine engine
Particulate matter
Diesel
Lubrication oil

ABSTRACT

Liquefied natural gas (LNG) is becoming increasingly popular as a marine fuel as emission regulations become more stringent. However, very little data are available on the particulate matter (PM) emissions of modern marine natural gas engines. In this study, we present a first detailed characterization of the composition of the PM emitted by a modern, in-use, natural-gas-powered vessel. The vessel engines use compression-ignition and only a small amount of diesel fuel as pilot. These engines drive electrical generators, providing propulsion as well as auxiliary power for the vessel. Our emissions characterization includes six different techniques to measure black carbon (BC), including all methods determined as appropriate for measuring BC emissions from ships by the International Maritime Organization, as well as particle size distributions, metal concentrations, and organic particulate emissions. PM emissions differed significantly between idle and at-sea operating conditions. At idle, PM emission factors were primarily organic (approximately 1500 mg/kWh), with BC emission factors over two orders of magnitude lower (5.6 ± 0.4 mg /kWh). At engine loads above 25%, all emissions were independent of load and substantially lower than at idle, at 4.4 ± 1.7 mg/kWh for organics and 0.8 ± 0.2 mg/kWh for black carbon. When operated only on diesel fuel, this engine emitted 8-fold more organic PM (38 ± 15 mg/kWh) and 37-fold more BC (30 ± 11 mg/kWh) at loads above 25%. At idle loads, the diesel-fuel emissions were comparable to the natural-gas emissions. In addition to organics and BC, a third category of non-volatile sub-10-nm particles was identified. A detailed consideration of our measurements indicated that the sources of the organic,

* Corresponding author.
** Corresponding author.
E-mail addresses: Joel.Corbin@nrc-cnrc.gc.ca (J.C. Corbin), Stephanie.Gagne@nrc-cnrc.gc.ca (S. Gagné).

https://doi.org/10.1016/j.atmosenv.2019.117030
Received 14 May 2019; Received in revised form 30 September 2019; Accepted 2 October 2019
Available online 9 October 2019

BC, and sub-10-nm particles were lubrication oil, diesel pilot fuel, and lubrication-oil metals, respectively. Future studies should seek to quantify the emissions of other dual-fuel engines that will be entering the market.

1. Introduction

Marine transportation is traditionally powered by non-renewable crude-oil fossil fuels, either residual or distillate, the availability of which is fundamentally limited (Korakianitis et al., 2011). Partly for this reason, attention has recently shifted to natural gas (NG), a mixture of gaseous fossil fuels typically containing approximately 90% methane, a small percentage of ethane, and traces of other alkanes and nitrogen (Korakianitis et al., 2011), which may be transported as liquefied NG (LNG). A far more urgent reason is the goal of reducing CO_2 emissions by at least 50% by 2050 in order to stabilize the climate (Boucher et al., 2013; Tartakovsky and Sheintuch, 2018). NG is considered to have the potential to contribute to such reductions because its low carbon-to-hydrogen ratio results in fewer moles of CO_2 produced per mole of NG combusted relative to heavier fossil fuels, and its lower heating value is slightly higher than that of gasoline or diesel (Korakianitis et al., 2011; Tartakovsky and Sheintuch, 2018). In the longer term, a transition from NG to sustainable biogas fuels may also be preferable to a transition from diesel to sustainable biodiesel (Bengtsson et al., 2012, 2013).

For sufficiently-rich combustion mixtures (Sommer et al., 2019), NG combustion generally produces substantially lower concentrations of particulate matter (PM) than traditional fuels (Korakianitis et al., 2011). This is because of its low number of carbon atoms per molecule, as well as its low carbon-to-hydrogen ratio (Tree and Svensson, 2007). The low carbon-to-hydrogen ratio of NG therefore reduces both its PM and its CO_2 emissions. Moreover, since NG is a gas, it is generally combusted after pre-mixing in the cylinder, resulting in a leaner stoichiometry and a lower combustion temperature compared to traditional fuels (like diesel), which generally burn near a stoichiometric ratio of unity (near maximum temperature) due to being spray-injected as liquids. These lower temperatures result in lower nitrogen oxide (NO_x) emissions. However, emissions of carbon monoxide (CO) and of total volatile hydrocarbons (TVHCs), particularly methane, tend to be higher for NG than for traditional fuels (Papagiannakis and Hountalas, 2004; Korakianitis et al., 2011). The mixture of gas-phase and PM pollutants emitted by NG combustion can therefore be expected to be substantially different to the emissions from traditional fuels. This is likely to result in a substantially different toxicity, as indicated by the very different biological effects observed between traditional fuels such as diesel and heavy fuel oil which have been observed on human lung cells (Oeder et al., 2015).

In addition to their harmful effects on public health, combustion emissions may adversely affect the environment through radiative forcing of the climate, deposition on snow, and potentially eutrophication or acidification (Bengtsson et al., 2011, 2013). The radiative forcing exerted by greenhouse gases such as CO_2 and methane generally act on a global scale, as the atmospheric lifetime of these gases ($\gg$ 200 (Archer et al., 2009) and 10 years (Jacob, 1999), respectively) is much longer than the 1–2 years they require to be mixed throughout the tropo- and stratospheres (Jacob, 1999). In contrast, PM exerts a regional radiative forcing as it has a short lifetime of only 1–2 weeks before being deposited to the surface (Jacob, 1999). If deposited onto snow, light-absorbing PM such as black carbon (BC) may continue to exert a radiative forcing (IPCC, 2007; Skeie et al., 2011; Skiles et al., 2018). The greater sensitivity of the Arctic to BC deposition is particularly noteworthy, as the Arctic currently faces substantial increases in marine traffic in upcoming decades due to retreating sea ice (Quinn et al., 2015), which has motivated ongoing discussions at the International Maritime Organization (IMO) to investigate BC emissions from marine vessels. Other regional effects of BC may include the formation (Coggon et al., 2012) or induced-evaporation of clouds (Menon et al., 2002).

The cetane number of NG is so low that it is not usually quoted (Korakianitis et al., 2011), meaning that NG engines must be either spark-ignited or compression-ignited using a high-cetane-number pilot fuel such as diesel. The percentage contribution of this pilot fuel to the total fuel energy is typically about 30% (Korakianitis et al., 2011), but is as low as 1% in modern marine NG engines such as the one studied herein. It is therefore not clear to what degree the results of previous studies on NG combustion (Korakianitis et al., 2011; Bullock and Olfert, 2014; Papagiannakis and Hountalas, 2004; Hajbabaei et al., 2013; Hallquist et al., 2013; Li et al., 2015; Jayaratne et al., 2011) are relevant to such NG engines. Moreover, there is a need for a more comprehensive emissions characterization of dual-fuel engines, as the following summary of existing NG studies on either road vehicles or marine vessels will demonstrate.

Very little information is available on the properties of the PM emitted by LNG-powered marine engines. Anderson et al. (2015) characterized particle number and gaseous emissions from a compression-ignition, LNG-powered ship and found that particles were generally volatile, with mobility diameters $<$ 50 nm after 20-fold dilution. Consistent with general trends for NG (Korakianitis et al., 2011), CO and total gas-phase hydrocarbons (HCs, as measured by flame ionization) emissions were higher for NG than diesel-fuel operation. In contrast, PM number, NO_x, SO_2, and CO_2 were lower for NG. PM mass, as estimated from Engine Exhaust Particle Sizer (EEPS) measurements, was also lower. However, as noted by those authors, the estimation of PM mass from EEPS measurements requires substantial corrections and assumptions to be made, which were not made in that study; these corrections are in addition to those required for other particle sizers (that is, the particle effective density discussed below). Finally, based on the trace-metal content of the PM, Anderson et al. (2015) hypothesized that the volatile fraction of NG-combustion PM originated from evaporated lubrication oil, and that the non-volatile fraction originated from metal oxides within the oil.

Another study on NG emissions from marine engines was recently published by Lehtoranta et al. (2019). They reported PM number and mass emission factors for marine engines operated on various fuels, including NG. For particle number over 23 nm ($PN_{>23nm}$), they reported 1 to 2 orders of magnitude lower emission factors for NG combustion, compared to marine gas oil (MGO) or marine diesel oil (MDO). These latter two fuels are both similar to diesel except for their higher sulfur contents. However, as acknowledged by those authors and discussed further in Discussion, this comparison is not valid, since burning NG results in almost all emitted particles being $<$ 23 nm. Lehtoranta et al. (2019) also reported PM mass emission factors as being significantly lower for NG than for MGO or MDO, but did not report load-resolved PM composition as we do here.

No other studies have measured the emissions of NG-powered ships, although recent studies on NG-powered road-vehicle engines are worth mentioning in the present context (Jayaratne et al., 2011; Alanen et al., 2015). Alanen et al. (2015) reported that significant numbers of non-volatile particles with diameters below 10 nm were present in a retrofitted gasoline engine running on NG. Jayaratne et al. (2011) concluded that the PM from NG combustion is largely volatile, and that methane and other HCs respectively represent the greatest risk to climate and public health from NG emissions. The introduction of a catalyst into the exhaust of an NG engine has been shown to reduce those HC emissions by a factor of 20–50, with a corresponding 20–30 fold reduction in genotoxic activity (Turrio-Baldassarri et al., 2006). Reliable measurements of black carbon (BC) concentrations from NG combustion have not been reported to our knowledge.

Here, we have performed a detailed characterization of the aerosol emitted by a dual-fuel engine primarily combusting NG for the propulsion of a commercial, in-use vessel. Our characterization focusses on the PM emissions, in particular, on quantifying the amounts of BC and organic carbon (OC) observed at different engine loads. We discuss volatile and non-volatile particle size distributions, the physical origin of BC and OC, the relative performance of various techniques used to measure BC, and the importance of these PM emissions in the context of co-emitted methane and HCs. Recommendations for the future use of NG engines are provided.

2. Methods

Measurements were taken aboard a commercial, in use NG-powered vessel in western Canada. The vessel is powered by two Wärtsilä 9L34DF engines with a power output of 4320 kW each. These engines are nine-cylinder, compression-ignition, dual-fuel, four-stroke diesel engines and were operated at constant speed and varying load to drive electrical generators. They have been in use for less than a decade. There are no auxiliary engines on this vessel. While the vessel stores its fuel as LNG, we refer to the fuel as NG where appropriate since the fuel is injected in gaseous form as NG. The NG is indirectly injected and ignited by a diesel-fuel pilot charge, which contributes $<$ 10% of the total derived energy at 10% engine load, and much less at higher loads. The diesel pilot fuel is injected by a common rail system. The engines are specifically designed for operation on NG, rather than being retrofitted, and are also capable of running entirely on diesel fuel. The engine meets Tier 3 emission standards in LNG mode and Tier 2 standards in diesel mode.

The measurements presented herein were taken on a single engine during normal operation of the vessel. The load of the engine was set to a desired value between 6 and 91% of the rated maximum of 4320 kW (Table 1), typically for 30 min, while any additional required power was provided by the second engine. The sequence of measured engine loads was varied randomly, rather than following a sequence of continuous increases or decreases, as illustrated in Fig. S2. The actual time spent at each load during commercial operation can be varied by the operator, as discussed further in Sommer et al. (2019). Both LNG (91–95% methane) and diesel fuels were used. The vessel normally operates with LNG. The diesel fuel used was ultra-low-sulfur diesel, and met Canadian standards of $<$ 15 ppm sulfur. We note that the vessel was operated within an Emissions Control Area.

The engine emissions were extracted from the exhaust stack at average temperatures above 350 °C, using the sampling configuration shown in Fig. S1. Three lines distributed the sample to multiple instruments, as summarized in Table 2. The first two lines were used by an AVL 415SE smoke meter (AVL LIST GmbH, Austria) and a Horiba PG350 portable gas analyzer (Horiba, Japan). The gas analyzer was tested for drift after every test point. The third line was heated with heating tape to 50–60 °C, connected to a sampling manifold of the design described in Gysel et al. (2017), diluted approximately sixfold with compressed, dried and activated-charcoal-filtered air, and then distributed to the remaining instruments. The total sampled flow (approximately 60 L min^{-1}) was less than the total available flow, and an excess flow of approximately 10 L min^{-1} was directed into an exhaust line. The dilution factor was determined as the ratio of background-subtracted CO_2 concentrations before and after dilution; the measured background CO_2 concentration was 454 ± 12 ppmv (mean ± SEM of multiple background measurements). While a dilution correction using NO_x would also have been possible, a better signal-to-noise ratio for CO_2 was observed due to the NO_x emissions in NG mode being lower than for traditional fuels. The sampling line length between manifold and instruments (2–4 m) was selected to give approximately comparable residence times of 2–4 s in each case.

Table 1
Parameters of the engine studied. IMEP = indicated mean effective pressure.

Parameter	Value
Power	4320 kW
Net IMEP	22 bar
Bore and stroke	340 and 400 mm
Displacement	36.3 l/cyl
Speed	720 rpm
Cylinders	9
Intake valves	2
Exhaust valves	2
NG injection	indirect

The remaining instruments included five BC instruments (described below), a scanning mobility particle sizer (SMPS, TSI, USA), two sets of filter samplers, two transmission electron microscopy samplers, a custom-built methane sensor, a CO_2 monitor, and a flame ionization detector for methane and non-methane HCs. The filter samplers were used to obtain quartz-backed-quartz and Teflon samples for thermal–optical carbon analysis (TOA; EUSAAR2 protocol (Cavalli et al., 2010)) and X-ray fluorescence spectroscopy (XRF) analysis, respectively. The filters which were analyzed by TOA were sealed and stored on ice prior to their measurement. The TEM samples were collected in duplicate using two different samplers, a thermophoretic sampler constructed at the University of British Columbia and an electrostatic sampler (ESPnano, DASH Inc., USA) (Miller et al., 2010), and were analyzed using a Hitachi H7600 at 80 eV acceleration voltage; a detailed analysis will be presented elsewhere (Trivanovic et al., 2019). The custom-built methane sensor utilized wavelength modulation spectroscopy and was validated in the laboratory as described by Sommer et al. (2019).

The SMPS (TSI model numbers 3088, 3082, 3081 and 3776) employed an X-ray charger and generally scanned the mobility-diameter range 6–170 nm. The SMPS data were monitored throughout the experiments and, when evidence of larger particles was present, the upper limit of the SMPS scans was extended to ensure that the majority of particles had been observed (in number space). A median SMPS scan time of 20 s was used; scans of up to 200 s were used to ensure that 20 s was adequately long. The SMPS was used to obtain number-based particle size distributions and to estimate concentrations of both total PM (after the factor of approximately 6 dilution) and non-volatile PM. Non-volatile PM was obtained after denuding at 623 K using a catalytic stripper (Catalytic Instruments GmbH, Germany, model CS015). The SMPS estimations of total PM mass are approximations, as the instrument is designed to measure number rather than mass. The major assumption required in estimating mass from SMPS measurements is that an effective density can be described, and that all particles were counted by the SMPS, as further discussed in Section 2.3. The more reliable measurement of total PM mass in this study was obtained from the carbon mass measured on the filters by thermal–optical analysis (TOA), as described below.

2.1. BC (eBC, rBC, and EC) measurements

Motivated by ongoing discussions at the IMO on measurement of BC and the investigation of BC control measures in the context of marine emissions in the Arctic, we deployed multiple instruments to measure BC during this campaign. BC is a complex material which is normally defined as consisting of aggregates of nano-spherules of refractory, insoluble, strongly-light-absorbing, sp^2-bonded graphitic carbon (Petzold et al., 2013; Bond et al., 2013). The preceding list of properties means that different measurement principles may be used to determine BC mass concentrations. In the following, we follow the recommendations of Petzold et al. (2013) and use technique-specific terminology when discussing the measurements of different BC instruments. The properties of the instruments described in this section are summarized in Table 2.

It is essential to note that some types of PM may possess properties (in terms of solubility, light absorptivity, refractoriness, and sp^2 bonding) which overlap with the above-mentioned defining properties

Table 2
Instruments used in this study and corresponding principles of measurement. DR = measured dilution ratio (rounded to the nearest integer in this table). eBC = equivalent BC, rBC = refractory BC, EC = elemental carbon, OC = organic carbon. [a]All eBC concentrations defined relative to a mass absorption cross section of 7.5 m^2 g at 550 nm, scaled to the measurement wavelength with an Ångström absorption exponent of 1.0 (Moosmüller et al., 2009). [b]This instrument was switched between two different lines.

Instrument	Abbrev.	DR	Measurand	Reported Quantity
Scanning mobility particle sizer	SMPS	6	Mobility size distributions of nascent and 623 K-denuded particles	$N_{6-170nm}$, $dN/d\log d_{mob}$
AVL 483 Micro Soot Sensor	MSS	6	In-situ aerosol light absorption (photoacoustic)	eBC[a] at 808 nm
ARI CAPS PM_{SSA} monitor	CAPS	6	In-situ aerosol light absorption (extinction-minus-scattering)	eBC[a] at 660 nm
DMT Photoacoustic Extinctiometer	PAX	6	In-situ aerosol light absorption (photoacoustic)	eBC[a] at 870 nm
AVL 415S Smoke Meter	SM	1.0	Light attenuation through PM-laden filter	eBC[a] at 560 nm
Artium LII300	LII	6	Laser-induced incandescence with two-color pyrometry	rBC
Quartz filter samples	–	6	Carbon evolution in inert and oxidizing gases, with optical correction for pyrolysis	EC, OC
Teflon filter samples	–	6	X-ray induced fluorescence	Metal concentrations
Horiba PG350 Gas Analyzer	–	(1.0, 6)[b]	CO, CO_2, NO_x, SO_2	Gas concentrations [ppmv]
LI-COR 850	–	6	CO_2, H_2O	Gas concentrations [ppmv]

of BC (Corbin et al., 1038). Since most BC measurement instruments rely on measuring only one of these properties, disagreement between different BC measurements may result for special cases of complex PM mixtures. In particular, for engines operated on heavy fuel oil, the presence of so-called tar and char PM will result in disagreement between instruments which aim to exploit either the light absorption, refractoriness, insolubility, or sp^2 bonding of BC (Corbin et al., 1038). (The only other special case is that of biomass-burning PM (Corbin et al., 1038).) The principles on which these instruments operate are defined in the following.

The most common measurand for BC is light absorption at a wavelength λ, which may be reported as equivalent BC concentrations eBC(λ) if a mass-specific absorption efficiency (MAE) is assumed (Moosmüller et al., 2009). In this study, the Photoacoustic Extinctiometer [PAX; Droplet Measurement Technologies, USA; eBC(870 nm)] (Nakayama et al., 2015), CAPS PMssa monitor [Aerodyne Research Inc., USA; eBC (660 nm)] (Onasch et al., 2015), Micro Soot Sensor [MSS, AVL GmbH Austria; eBC(808 nm)] (Schindler et al., 2004), and smoke meter [eBC (560 nm)] (Northrop et al., 2011) all measured and reported eBC assuming the MAE of 7.5 $m^2 g^{-1}$ at $\lambda = 550$ nm recommended by Bond et al. (Bond and Bergstrom, 2006). For each instrument, this MAE is converted to the measurement wavelength by assuming a wavelength-independent refractive index, from which it follows (Moosmüller and Arnott, 2009) that $MAE(\lambda_i) = MAE(550\ nm) \cdot 550\ nm/\lambda_i$.

The eBC instruments were calibrated as follows. The scattering detectors of the PAX and CAPS were calibrated on-site using non-absorbing aerosol (ammonium sulfate), according to the manufacturer's instructions. The absorption coefficient of the PAX was additionally calibrated with nebulized Aquadag (colloidal graphite). The MSS and smoke meter were not calibrated on-site. The MSS is calibrated against EC (defined below), although its principle of operation is identical to the PAX. The smoke meter measures the attenuation of green light ($\lambda = 560$ nm) through a PM-laden filter and reports filter smoke numbers (FSN), which were converted to eBC concentrations by the instrument software using the manufacturer's calibration (provided in the supplement as Equation S(1)).

Two other BC measurement techniques were employed. First, laser-induced incandescence (LII) was employed by the Artium LII-300 (Artium Technologies, CA, USA). This involves heating particles to approximately 3000 K with a high-fluence laser and measuring the intensity of laser-induced incandescence (LII) that results. From this intensity measurement, together with a two-colour-pyrometry measurement of temperature and literature knowledge of the BC absorption function $E(m)$, a measurement of BC known as refractory BC (rBC) (Petzold et al., 2013) can be retrieved as a mass concentration. The LII detectors are calibrated with a spectral radiance standard and the overall rBC quantification is calibrated against EC, as described by Snelling et al. (2005).

Second, thermal–optical analysis (TOA) was employed for the quartz-fibre filters, using a bench-top Sunset analyzer (Model V5) calibrated with sucrose and following the EUSAAR2 protocol, which is designed to minimize potential artifacts (Cavalli et al., 2010). Filter punches (area 1cm^2) were first heated in helium to desorb volatile carbon (the so-called organic carbon or OC mass) before the remaining carbon residue (the so-called elemental carbon or EC mass) was combusted in 2% oxygen. Because some OC may pyrolyze during analysis, transmittance (and reflectance) of a 630 nm laser through the filter punch is monitored throughout. In this study, pyrolysis was observed to be negligible in general.

When analyzing a first filter taken during NG operation at engine-idle conditions, we observed that the OC concentrations were extremely high and resulted in saturation of the TOA analyzer detectors. This occurred because filter sampling times were calculated according to the desired BC concentration, rather than the OC concentration. We therefore performed two separate experiments to determine OC concentrations at idle. First, we performed an isopropanol extraction of an idle-load filter before performing EUSAAR2 analysis, and found that the results were in excellent agreement with the consensus value discussed below. Second, we modified the EUSAAR2 protocol by adding an additional, slower heating step between the first and second stages of helium-atmosphere desorption in order to quantify carbon on these filters. This second experiment was performed to avoid detector saturation and allowed us to quantify OC concentrations at idle by subtracting the total evolved carbon from the EC determined from the extraction, as recommended by the VDI 2465/1 protocol (Schmid et al., 2001).

The OC concentrations at idle were also estimated using the SMPS data. At idle, the uncertainties associated with estimating mass from SMPS measurements were lowest, since the single scattering albedo (ratio of scattering to extinction coefficients) measured by the CAPS PMssa showed that a large fraction of the PM mass was OC, reducing the uncertainty associated with the assumption that particles were spherical. However, agreement between SMPS and OC at idle was still poor (Fig. S7) and we rely on the SMPS-estimated mass below for qualitative interpretation only.

2.2. Calculated quantities

Engine emission factors EF_m, in terms of PM mass emitted per kWh produced, were calculated as

$$EF_m = \frac{[PM]_m \cdot Q_{exhaust}}{P} \quad (1)$$

where $[PM]_m$ is the mass concentration of a PM species in $mgNm^{-3}$, $Q_{exhaust}$ is the engine exhaust flow rate (measured in-situ for a given test point with a pitot probe) in $Nm^3\ h^{-1}$, and P is the engine power in kW reported by the engine control software. All concentrations were corrected to standard conditions of 273 K and 1 atm. We have considered the engine exhaust flow and power measurements to have negligible

uncertainty.

Equation (1) can also be used to calculate number-based EFs, if the quantity $[PM]_m$ is replaced by $10^6[PM]_n$, with $[PM]_n$ given in units of particles per cm^3.

Measured size distributions were corrected for losses in the catalytic stripper by multiplying the measured values with a penetration function provided by the manufacturer, which was itself derived through a combination of theory and empiricism (personal communication, Catalytic Instruments, 2018).

Particle penetration through our sampling system was modelled using the software published by von der Weiden et al. (von der Weiden et al., 2009). At 10, 20, 40, 100 nm penetration to the SMPS was 73, 85, 91, 95%. The size-resolved penetration is shown in Fig. S5 in the context of the particle volume distribution calculated from the SMPS data for each engine load. Comparison of the penetration function and volume distribution shows that the majority of BC (largest mode) will have been measured with approximately 95% penetration, whereas OC will have been measured with approximately 75% penetration and the small involatile mode discussed below will have been measured with approximately 60% penetration. We have not corrected the values reported below by these penetration estimates.

No loss correction for the remainder of the sampling lines was made. As there were no small-angle bends in that sampling line, such losses would be dominated by diffusion to the tubing walls, which (for 5 $Lmin^{-1}$ flowing through 2.5 m of tubing) fall from 99% at approximately 100 nm mobility diameter to 50% at about 20 nm and 20% at about 11 nm (Kulkarni et al., 2011). The corresponding losses of the smallest mode of particles measured below 20 nm would therefore be substantial. However, as our sampling system was not designed to quantify such particles, we have not attempted to perform a correction.

2.3. Uncertainties

In general, error bars are reported as the standard error of the mean (SEM, representing variability in the specific measurement point). Mean values (such as emission factors) are reported together with their standard deviations (representing the spread of measured values). Repeated measurements of specific engine loads are plotted separately to illustrate the observed variability in engine emissions.

When calibration uncertainties were analytically available (CAPS, PAX, CO_2 monitor) they were added in quadrature to the statistical imprecision, as described in the following. The span value of the CO_2 monitor was checked at the beginning and end of each day using a 14.42% CO_2 reference mixture; the measured value was always within ± 2% of the reference value. This ±2% was therefore propagated into the CO_2 uncertainty. (No absolute-value CO_2 uncertainty is necessary, since all measurements were of high CO_2 concentrations (Wilson et al., 2004).) The CAPS calibration results in a single scattering-coefficient calibration factor, which is obtained by the slope of a weighted least-squares fit; the corresponding uncertainty in the fitted slope was propagated into the uncertainties reported here. The PAX calibration results in an analogous slope and a similar procedure was applied. As no other instruments were calibrated on-site, no other calibration uncertainties were treated explicitly. Overall, statistical uncertainties were generally smaller than the symbols in the plots shown below, with the exception of some SMPS data. Unquantified uncertainties, such as the potential measurement biases between BC instruments, are considered qualitatively by comparing instruments when possible.

Special uncertainties are worth mentioning for certain instruments. In general, the quantities presented below were measured analytically. The exception is the SMPS-estimated mass concentration, which was estimated by treating all measured particles as spheres with an assumed effective density. This density is described as effective because it requires the assumption of particle sphericity. Previous studies (Park et al., 2003; Gysel et al., 2012) have measured the effective density of typical

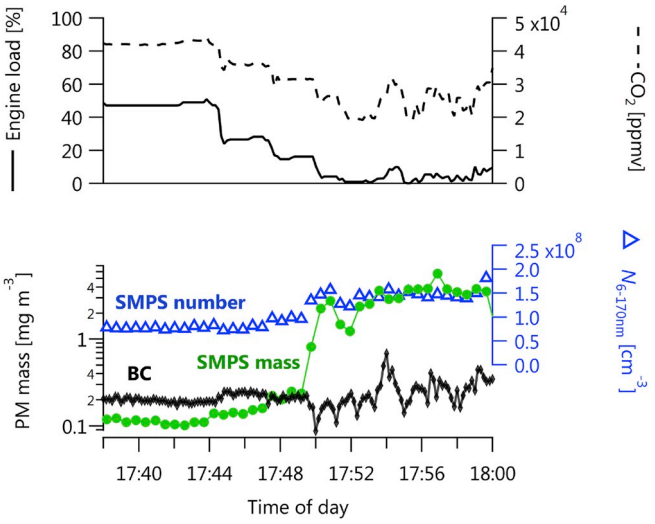

Fig. 1. Dilution-corrected time series of BC, CO_2, and SMPS-measured particle number and mass concentrations during transition from high load to idle. Note the increased variability in BC at idle, which is due to cylinder deactivation (see also Fig. 6). The BC mass concentrations represent the median of all BC measurements. At loads greater than 20%, the SMPS-estimated mass concentration is smaller than the BC mass concentration due to the inaccuracy of the assumed particle shape and density (Section 2). Error bars are omitted for clarity and generally smaller than the data symbols.

BC particles in the size range discussed below as 700–900 kg m^{-3}, and the particles observed in our study are consistent with this range (Trivanovic et al., 2019). For an NG-powered engine, Bullock and Olfert (2014) reported a mean effective density of 850 kg m^{-3} under conditions where > 95% of the PM was volatile. Bullock and Olfert also reported that this density is similar to that of lubrication oil. Here, we have used an effective density of 850 kg m^{-3} for all engine conditions, which serendipitously applies to both OC and BC particles, according to the discussion above. We note that the uncertainty of this effective density is greatest for BC, and estimate a 25% uncertainty in the accuracy of all SMPS-derived mass concentrations. The corresponding error bars shown below do not include this 25% and reflect statistical variability only.

3. Results

3.1. Overview of NG-mode engine emissions

A typical time series of the engine output is shown in Fig. 1. The figures shows a period of rapid changes in engine load as the vessel was manoeuvred close to shore. This time period was selected to highlight several features of the engine: stable emissions at engine loads above 20%, variable BC concentrations at lower engines loads, and the emission of substantial amounts of volatile PM at lower engine loads. A full-day time series version of this figure is shown in Fig. S2. For the engine loads analyzed in detail below, the engine was fixed at certain loads for longer periods of time (median 48 min, maximum 100 min) as shown in detail in Table S1 over the course of three days.

The increase in variability of BC concentrations at lower engine loads in Fig. 1 is shown by all four real-time BC instruments (CAPS, LII-300, MSS, and PAX). This variability corresponds to the triggering of a cylinder-deactivation strategy by the engine-control software at engine loads below 15%. This cylinder-deactivation strategy entails deactivating LNG injection to two of the nine engine cylinders to increase combustion efficiency and therefore substantially reduce methane emissions (Sommer et al., 2019). Diesel pilot fuel is still injected in all cylinders.

A substantial increase in volatile PM emissions was observed at lower engine loads, as evident from the SMPS data shown in Fig. 1. The figure shows the integrals of the first (number) and third (volume) moments of

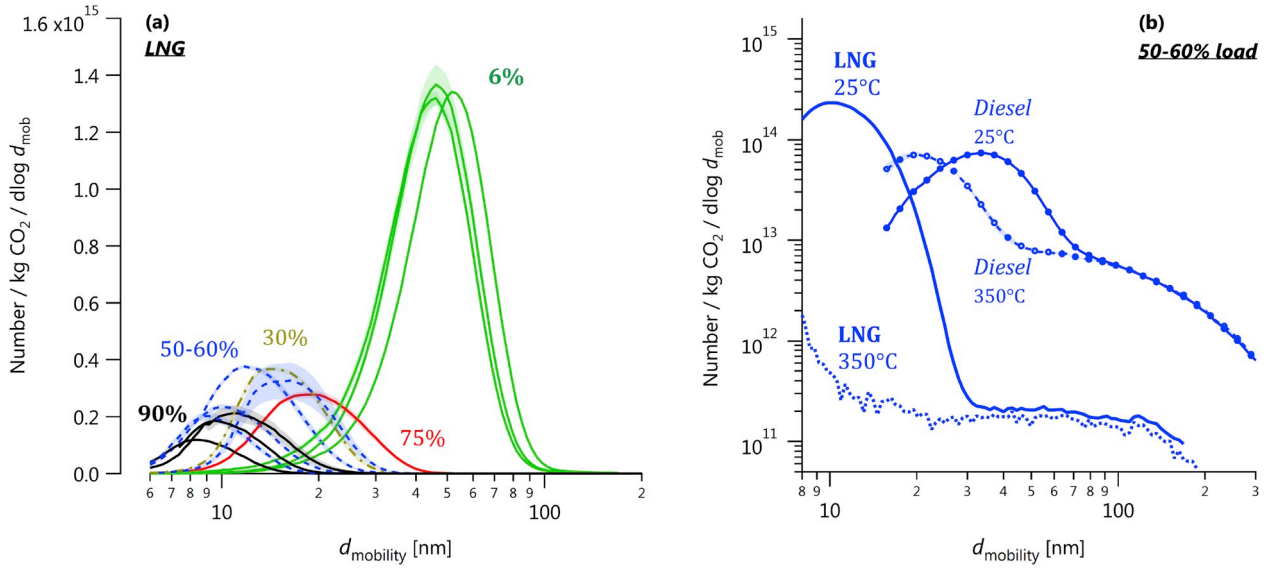

Fig. 2. (a) Mobility size distributions as a function of engine load in LNG mode. (b) Mobility size distributions at 50% load for diesel and LNG modes, with and without the removal of volatiles at 623 K by the catalytic stripper. Note that, since (b) shows that the majority of particles in (a) were volatile, the larger sizes observed at 6% load can be understood to indicate that volatile (organic) emissions were higher at 6% load, as discussed in the text. For the same reason, smaller sizes would have been measured at higher dilution ratios. Note also that the mobility diameter of a soot particle is larger than that of an equivalent-volume sphere due to shape effects (Kulkarni et al., 2011).

the SMPS size distributions, labelled as $N_{6-170nm}$ and (after weighting by an effective density of 850 kg m^{-3}) mass concentration. It is clear that the total PM mass increases substantially immediately after the engine load fell below approximately 15%, As discussed further below, this increase in PM mass is attributable to organic PM, since BC concentrations remained constant and the LNG fuel was sulfur-free.

We emphasize that, since the vessel studied here was a roll-on/roll-off ferry with a relatively short route, it spent a considerable amount of time at idle, in contrast to the standard ISO 8178-E2 engine testing cycle used for heavy-duty, constant-speed engines for ship propulsion (which assigns weights of 0.15, 0.15, 0.5, and 0.2 to engine loads of 25, 50, 75, and 100%). We therefore considered these high idle emissions in detail below, as was also done in Sommer et al. (2018). The reader is referred to Sommer et al. (2018) for further discussion on the relative time spent at different loads by this vessel.

3.2. Size distributions and TEM of volatile and non-volatile particles

Fig. 2a shows the mobility-size number distributions measured at various loads for LNG-mode operation. The number distributions are generally log-normal with a mode diameter of 10–20 nm at engine loads $\geq$ 30 %, and 50 nm at 6% load (idle) load. Repeated measurements at higher loads indicated a substantial variability in mode diameter, which is discussed further in Section 4 below. Fig. 2b shows that the primary particle mode at 50% load evaporated upon heating to 623 K; this 10–20 nm mode was therefore composed of organic PM and not BC.

The larger non-volatile particles shown in Fig. 2b were typical soot aggregates, as shown by the TEM micrographs presented in Fig. 3a–c. These examples were selected to be representative of a detailed TEM analysis of soot from this engine (Trivanovic et al., 2019). Note that the TEM images do not include the most abundant particles in the PM,

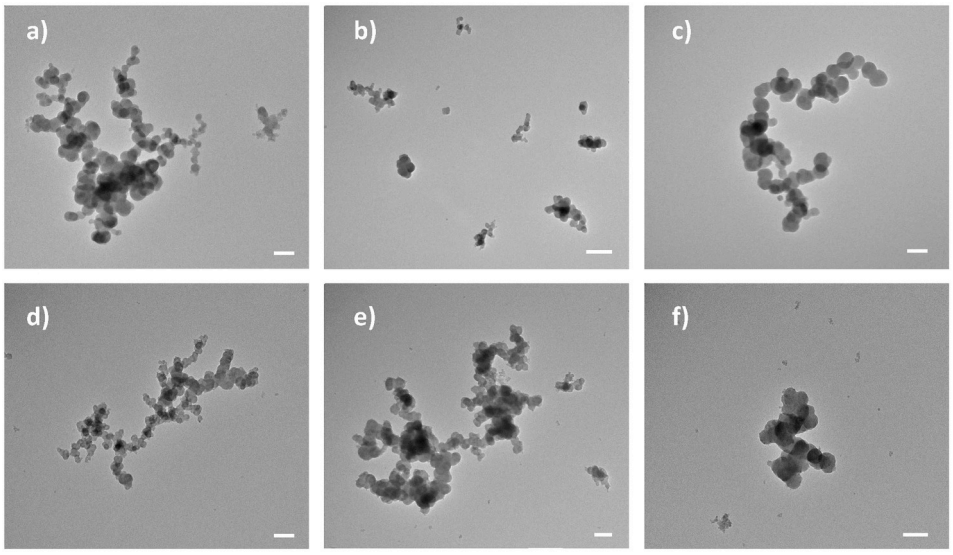

Fig. 3. Transmission electron micrographs of representative non-volatile particles sampled when operating in (a–c) LNG mode and (d–f) diesel mode. Note that the organic PM fraction will have evaporated within the vacuum of the microscope. Note also that these images do not represent the extremely-small (< 10 nm) non-volatile particles shown in Fig. 2b and discussed in the text.

which dominate the particle number distributions in Fig. 2a, because those particles were volatile.

The TEM images also do not represent the extremely small (< 10 nm) non-volatile particles visible in Fig. 2b. These particles remained visible after heating to 623 K, and were not partially-evaporated organics: their size did not grow when the heating temperature was reduced from 623 K to either 473 or 548 K (Fig. S3). We therefore hypothesize that these particles consisted of nucleated metal-oxides (Mayer et al., 2010) from the lubrication oil.

We emphasize that the measured mass (and size) of organic PM is a function of the amount of dilution employed prior to its measurement (Lipsky and Robinson, 2006; Swanson and Kittelson, 2009). Correspondingly, the larger particles measured at 6% load should be interpreted as caused by the higher overall organic PM mass concentrations. The potential cause of these higher organic emissions at lower load is discussed further in Section 4. Particle volume distributions corresponding to Fig. 2a are shown in Fig. S5.

When operating the engine with diesel fuel, the particle size distribution was substantially larger and bimodal, corresponding to the emission of BC-dominated rather than organic-dominated PM. Fig. 2b shows the diesel-fuel size distributions at 50% load, for total and non-volatile particles; Fig. S6 shows the distributions at all loads. The smaller mode was volatile, and corresponded to organic PM, whereas the larger mode was non-volatile, corresponding to BC.

3.3. Number, BC, and OC emission factors

Fig. 4a shows the measured emission factors, per kWh, of the present engine in LNG mode. The BC- and number-based emission factors were constant for loads above idle. Organic PM emissions were greater than BC emissions, at 4.4 ± 1.7 mg/kWh (mean ± SD) for organic PM compared to 0.8 ± 0.2 mg/kWh for BC. However, the BC particles were much larger than the organic particles, such that light scattering from the organic PM was relatively minor and the aerosol SSA at 660 nm was generally dominated by BC; the measured SSA of approximately 0.2 (Fig. 5) at higher loads is consistent with literature values for BC-only

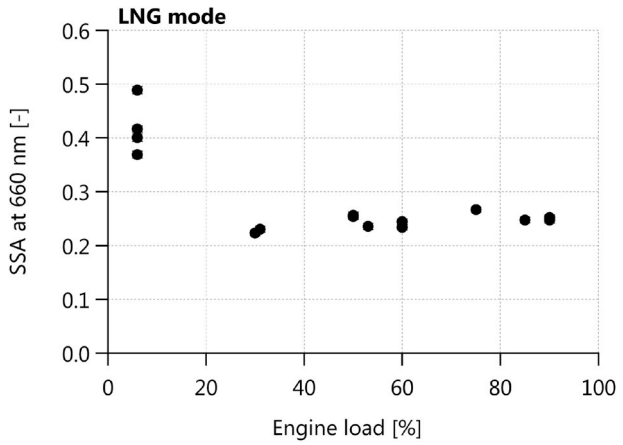

Fig. 5. The single-scattering albedo (SSA; ratio of scattering to extinction coefficients) of the aerosol at 660 nm, measured by CAPS PM_{SSA} as a function of engine load. The asymptotic value of ~0.2 is typical of BC (Bond and Bergstrom, 2006). Higher values at lower engine loads correspond to increased organic PM concentrations. Error bars are smaller than the data symbols. Corresponding diesel-mode data are not available.

aerosols (Bond and Bergstrom, 2006). At lower loads, this SSA was as high as 0.5, due to the correspondingly larger size of organic PM (Fig. 2a).

Fig. 4b shows the same data as Fig. 4a for diesel-powered operation. Switching from LNG to diesel mode, the BC emission factors at higher loads increased by over an order of magnitude, from 0.8 ± 0.2 to 30 ± 11 mg / kWh (mean and relative standard deviation of all BC measurements for ≥ 30% load). Idle emissions of BC were not changed by fuel switching, and were 5.6 ± 0.6 mg/kWh in both LNG and diesel modes. Idle emissions of organic PM were extremely high in both modes, (1450 ± 75 and 518 ± 28 mg/kWh in LNG and diesel modes respectively) as shown in Fig. 4b. At higher loads, particle number emissions were somewhat higher in LNG mode ($(6.9 \pm 2.7)\ 10^{13}$ kWh^{-1})

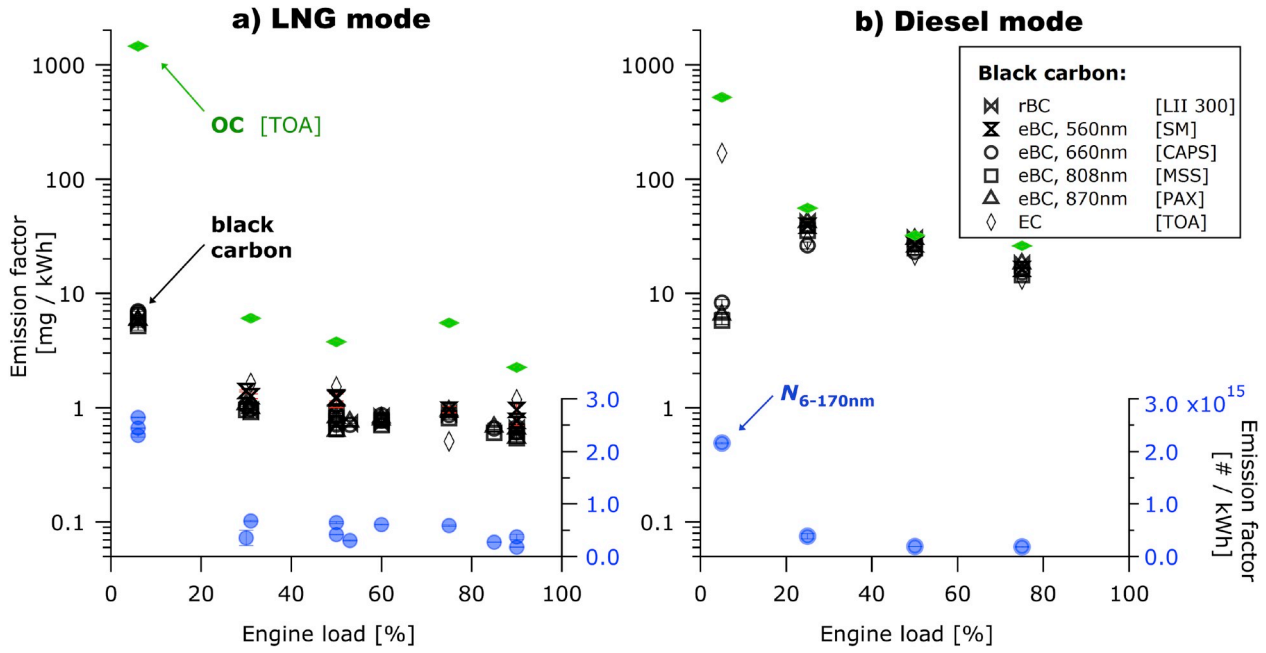

Fig. 4. Emission factors per kWh versus load for BC, total PM. (a) LNG mode, (b) diesel mode. Number emission factors measured by SMPS are plotted on the right ordinate; mass emission factors for BC (measured as eBC, rBC, or EC) and OC are plotted on the left ordinate. The positively-biased outlier in EC in panel (b) may be due to high OC concentrations; the corresponding measurement in panel (a) was performed after solvent extraction. Error bars are plotted, but are smaller than the data symbols. The number of repetitions at each load can be observed from the overlap of the $N_{6-170nm}$ symbols (blue circles). (For interpretation of the references to colour in this figure legend, the reader is referred to the Web version of this article.)

compared to diesel mode ($(3.8 \pm 1.7)\ 10^{13}$ kWh^{-1}). In both cases, these values were an order of magnitude higher at idle ($(3.8 \pm 0.2)\ 10^{14}$ kWh^{-1} for LNG mode, $(3.3 \pm 0.3)10^{14}$ kWh^{-1} for diesel mode), due to the higher OC emissions. SSA measurements for diesel mode were not available as the BC concentrations were above the upper limit measurable with the CAPS PM_{SSA} at the dilution levels employed herein.

3.4. Consistency between BC measurements

A major goal of the present study was to investigate to what extent different techniques for measuring BC would be reproducible for LNG-mode emissions. The very small scatter between BC instruments in Fig. 4a shows that all instruments performed consistently. The similarity in scatter between Fig. 4a and b indicates that the performance under LNG- and diesel-modes was comparable, in spite of a factor 50 higher BC concentrations in diesel mode. Fig. S4 allows a more detailed comparison of the instrument performances by plotting the ratio of each instrument to an arbitrary reference instrument as a function of BC mass concentration. These ratios were generally within the range ± 20%, with two exceptions: the ratio for the AVL 415SE Smoke Meter increased to approximately 2 at mass concentrations below 30 μg m^{-3}; and the ratio for the CAPS PM_{SSA} became meaningless at mass concentrations above 800 μg m^{-3}, as this instrument is not capable of measuring such high concentrations. The lower detection limit of the Smoke Meter, according to its manual, is 20 μg m^{-3}. While in our data set, the instrument accuracy suffered at concentrations slightly above this limit, we also note that the instrument accumulates PM prior to each measurement, so that a change of sampling configuration could improve its accuracy at lower concentrations, in future work.

4. Discussion

4.1. Comparison with related studies

As data on the emissions of LNG marine vessels are very scarce in the literature, here we discuss the only two studies we are aware of, those of Anderson et al. (2015) and Lehtoranta et al. (2019).

Anderson et al. (2015) (Wärtsilä 8L 50 DF) studied an engine that was slower (514 rpm) than the engine we studied here (720 rpm), with a longer bore and stroke (500 and 580 mm) than the engine we studied (340 and 400 mm). Its maximum mechanical output is 15,600 kW, compared with 4320 kW for the engine we studied.

Anderson et al. (2015) reported number emission factors that were independent of load, for loads above 30%, with a mean value of approximately 5×10^{12}kWh^{-1}, over two orders of magnitude lower than our corresponding mean and standard deviation of $(4.4 \pm 1.7) \times 10^{14}$kWh^{-1}. Note that although our measured size range, 6–170 nm, was smaller than theirs, 5.6–560 nm, the measured size distributions in both cases indicate that the instruments counted the majority of particles.

Anderson et al. (2015) also estimated non-volatile PM mass emission factors from these number-distribution measurements at > 30 % load as approximately 0.15 mg/kWh, substantially smaller than our corresponding value of 0.79 ± 0.17 mg/kWh. We consider this difference as much greater than the uncertainty in the data sets. Overall, the emission-factor differences between the engine studied by Anderson et al. (2015) and the engine we studied highlight the extent to which emission factors may vary with engine design parameters.

Lehtoranta et al. (2019) studied multiple engines. They reported the total-PM emission factors for NG as significantly less than MDO and MGO, similar to our results for diesel. Our measured emission factors are slightly lower than theirs. For example, at 85% load for a Wärtsilä Vasa 4R32 engine (750 rpm, 320 mm bore, 400 mm stroke), they reported a total PM emission factor of 9 mg/kWh for NG, which is roughly comparable to our typical high-load value of 5.2 ± 1.7 mg/kWh (this value and uncertainty represent the sum of the mean values we reported in Section 3.3 for OM and BC). Lehtoranta et al. (2019) also reported total-PM emission factors of {20, 32, 9} mg/kWh at respective loads of {40%, 75%, 85%}. These results suggest that in their study, as in ours (Fig. 4), the engine emissions did not follow a clear trend with load.

Lehtoranta et al. (2019) also reported particle-number-based emission factors for diameters greater than 23 nm, $PN_{>23nm}$. They measured $PN_{>23nm}$ because this quantity is part of the Stage V European Union regulations, which will be applicable in the year 2020. (The value of 23 nm is ultimately traceable to the Particle Measurement Programme, PMP, developed for the measurement of emissions from ground vehicles.) Our measurements show that the majority of particles emitted from NG combustion in marine vessels are < 23nm; therefore future regulations should be revised to include smaller particles in order to properly address NG emissions. We measured PN emissions > 10^{13} particles/kWh, over an order of magnitude greater than the Stage V regulations of < 10^{12} particles/kWh (for $PN_{>23nm}$). However, these emissions would have been below the limit if we had only measured $PN_{>23nm}$, particularly at higher loads (Fig. 4). The work of Alanen et al. (2015) indicates that this conclusion applies not only to marine vessels, but also to passenger cars. We reiterate here that volatile organics comprised these NG-related particles, and therefore we would have observed even smaller particles at the smaller dilution ratios of 10 which Lehtoranta et al. used, compared to our dilution ratio of 6.

4.2. Origin of PM emissions in LNG mode

In LNG mode, both BC (Fig. 4) and CO_2 (Fig. S8) emission factors were constant as a function of engine load, for loads ≥ 30%. At lower engine loads, decreased combustion efficiency has been highlighted as leading to methane emissions due to a decreased burnoff of injected methane (Sommer et al., 2019). Our data show that this decreased combustion efficiency also corresponds to enhanced emissions of organic PM and BC. These enhanced emissions may be attributed to a decreased burn-off of the PM, as predicted by theory (Korakianitis et al., 2011).

BC emissions were constant at all other loads, which leads to the hypothesis that the primary source of BC was the diesel-fuel pilot injection. For example, the fuel-rich regions in which soot formation occurs (Tree and Svensson, 2007) would be more likely to form close to the droplets of this pilot diesel fuel. We tested this hypothesis by considering

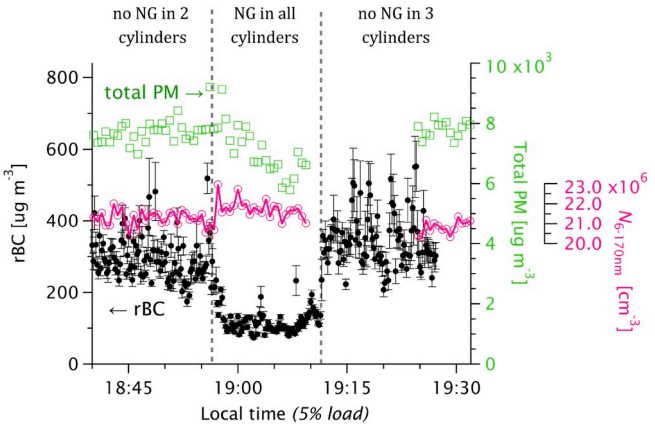

Fig. 6. Effect of skipping methane injection on rBC and total PM (estimated by SMPS in terms of both mass and number) concentrations in LNG mode at idle (load 5.4 ± 0.4 %, mean and standard deviation). rBC concentrations were higher and more variable when methane (CH_4) was not injected into the cylinder, suggesting an origin of incomplete pilot-diesel-fuel oxidation. Total PM concentrations decreased only slightly, and with a slow response, when changing injection conditions. Note that the cylinders into which methane was not injected were varied rapidly at each condition.

an experiment in which the number of deactivated cylinders under idle conditions was varied. As shown in Fig. 6, either two (the default number during this study), zero, or three cylinders were deactivated. Each cylinder was deactivated for a short time period only, as controlled by the engine software. The figure shows that injecting NG into all cylinders (middle case) resulted in lower BC emissions than deactivating NG injection into two or three cylinders. In other words, BC emissions increased when increasing the ratio of diesel to NG fuel in the cylinders. The observed near-instantaneous decrease in BC suggests that the diesel pilot fuel serves as a source of BC whereas the NG serves as an overall sink by increasing burnoff. We assume here that potential differences in fuel injection timing during cylinder deactivation conditions were negligible; we did not have access to this information in this study.

Deactivating three cylinders instead of two led to slightly more BC. Also, BC concentrations were more variable during cylinder deactivation, on a timescale of seconds. Since cylinder deactivation involved rapidly switching which two or three cylinders were deactivated, this variability indicates that the switching process directly influenced BC emissions. Variability in the organic PM emissions occurred on a different timescale. Rather than a rapid variation, a slow decrease on a timescale of several minutes is observed in Fig. 6 after a change in cylinder deactivation strategy. This slow decrease indicates that the organic PM did not originate directly from the NG but from some mechanism associated with the engine operation or equilibration, such as the evaporation of lubrication oil. Neither organic PM mass nor number concentrations were affected by cylinder deactivation (Fig. 6).

Organic PM emissions at lower loads were an order of magnitude greater than BC emissions for both diesel- and LNG-mode operation, in terms of mass-based emission factors. These emissions were almost negligible at higher engine loads (Figs. 4 and 5) for both NG and diesel mode. These condensed-phase organics therefore likely originated from lubrication oil, based on the following four lines of evidence: (i) their independence from NG injection (Fig. 6), (ii) the similar patterns of organic PM emissions between the two fuel modes, (iii) the observed volatility of the organic PM (Fig. 2 and S3), and (iv) the fact that only Zn and Ca (both associated with lubrication oil) were present in the PM at detectable concentrations (Table S2 and discussion below). This conclusion is corroborated by literature evidence (Bullock and Olfert, 2014) of the organic PM density being similar to that of lubrication oil. The predominance of organic PM over BC emissions indicates that the climate forcing of NG exhaust is mainly influenced by the organic PM and by emissions of methane gas (Sharafian et al., 2019), which were also substantial in our study (Figs. S8 and S9).

Finally, our data show that BC and organics are not the only PM found in the NG exhaust. A particle type with mode diameter < 10nm was observed after a 623 K (350 °C) catalytic stripper removed all volatile material (as verified experimentally; Fig. S3). Therefore, these particles cannot be organics. These particles form a second mode in the non-volatile size distribution (Fig. 2) relative to the larger BC mode at 100 nm diameter. It is therefore most likely that this small, non-volatile particle mode represents metal oxides formed by combustion of the lubrication oil. Such particles have been observed previously in diesel-engine exhaust (Mayer et al., 2010). In support of these conclusions, we note that separate transmission-electron-microscopy measurements of the present samples showed that BC particles had typical aggregate sizes that were much larger than 10 nm (Trivanovic et al., 2019) and that the X-ray fluorescence elemental-composition measurements (Table S2) showed that trace metals associated with lubrication oil (Zn, Ca) were the only metals present in the PM with mean concentrations greater than the detection limit. Furthermore, the ratio of these two metals was not statistically different between the two fuels (4.4 ± 1.7 for six LNG-mode samples and 5.3 ± 3 for seven diesel-fuel samples).

4.3. Environmental implications

Our results are relevant to three environmental domains: direct global radiative forcing, BC deposition on snow, and public health.

The radiative-forcing effects of greenhouse gases are often summarized using the global-warming potential metric (GWP) (IPCC, 2007). GWPs are calculated by scaling emission factors up by a constant factor. This is a limited metric for multiple reasons, the most important being that the choice of GWP timescale strongly influences its interpretation (Pierrehumbert, 2014). Other reasons include the treatment of emissions as pulsed and the fact that aerosol-climate effects are complex (Pierrehumbert, 2014; Allen et al., 1038; Bond and Sun, 2005). The technology warming potential (TWP) is a significantly-improved metric (Thomson et al., 2015). Nevertheless, we calculated the 100-year GWP of CO_2, methane (GWP_{100} of 28 (IPCC, 2007)), and BC (GWP_{100} of 900 (Bond et al., 2013)) using our CO_2 and BC data in combination with the methane emissions from this vessel measured simultaneously with our data and reported by (Sommer et al., 2019). We found that the GWP of BC was negligible relative to CO_2 and methane, as illustrated by the fact that it is not visible in a plot of these GWPs (Fig. S9). This result is due to the much shorter atmospheric lifetime of BC relative to methane and CO_2 (Pierrehumbert, 2014). However, the short atmospheric lifetime of BC means that it is deposited onto the planetary surface within approximately 10 days (Jacob, 1999), where BC may continue to exert climate forcing, for example by lowering the albedo of snow and ice. These continued climate effects are not taken into account by the GWP.

We illustrate the potential snow-albedo impacts of BC emissions in Fig. 7, where the emission factors reported in Fig. 4 have been weighted according to the ISO 8178 E2 cycle and expressed as emission rates. We have not converted these emission rates into snow albedo reductions as the relationship is complex, being influenced by sublimation, precipitation, atmospheric processing, and snow aging (IPCC, 2007; Skeie et al., 2011; Skiles et al., 2018). However, higher emission rates are directly associated with greater snow-albedo reductions. Therefore, our results suggest that the use of NG is favourable over diesel or residual fuels in regions such as the Arctic, where BC deposition may affect climate.

It should be emphasized here that engine tuning and operation may play a large role in the emissions of a particular engine, and that some diesel engines may emit less BC per kWh than observed here. With regard to operation, the operator of the commercial vessel measured in this study has already modified its daily operations such that the engine is not idled at shore; hotel power is rather obtained from shore power. Further improvements, in collaboration with the engine manufacturer,

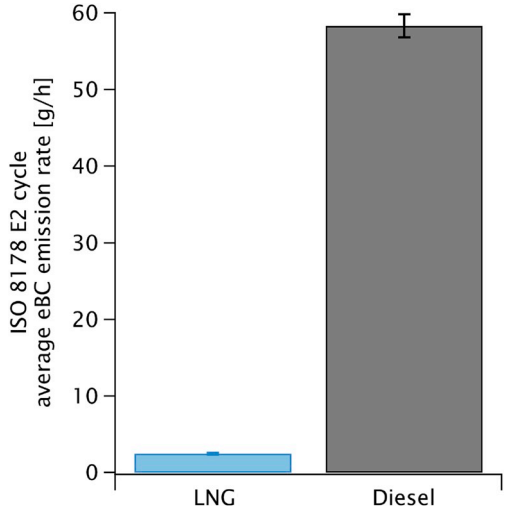

Fig. 7. BC emissions averaged over the ISO 8178 E2 Cycle in units of g BC emitted per hour. The E2 cycle weights emissions at loads of {25%, 50%, 75%, 100%} by factors of {0.15, 0.15, 0.5, 0.2}; we have used data from the nearest available loads (Fig. 4) for this calculation. BC deposition onto snow and/or ice is directly related to this emission rate, in addition to depending on atmospheric processing and precipitation.

are expected to be possible, as the present data set reflects the performance of this engine after initial deployment of this relatively-new technology.

With regard to health effects, three issues must be noted. Diesel-fuel exhaust has been statistically associated with lung cancer (Benbrahim-Tallaa et al., 2012; Pallapies et al., 2013; Sun et al., 2014), and mechanistic studies have shown that exhaust toxicity is related to the non-volatile component of the PM (Pan et al., 2004; McWhinney et al., 2013). Therefore, the decrease of BC in LNG-mode operation versus diesel-mode operation must correspond to a decrease in certain toxic species. The overall toxicity of the emissions of this engine, considering BC, formaldehyde, and particle number emissions, must be evaluated in future studies. In addition to the effects of combustion emissions, the total environmental costs of fuel production and transport must be considered for both fossil fuels and sustainable fuels. In this context, we note that Bengtsson et al. (2013) found that liquefied gaseous fuels including LNG and liquefied biogas were the most preferable fuels for short-haul sea shipping.

5. Conclusions

A comprehensive characterization of the particulate matter (PM) emitted by a modern dual-fuel, LNG-powered vessel was performed. The emission factors of organic PM and BC were determined, compared with those of CO_2 and methane, and discussed in terms of the origin of the PM species. Size distributions of total and non-volatile (solid) PM were also reported. Volatile PM had a mode number distribution of approximately 50 nm at idle loads and 10–20 nm at loads above 25%. Non-volatile PM particles were measured with two modes, one above 100 nm and one below 10 nm. Based on TEM evidence, the larger mode was BC; the smaller mode most likely contains metal-oxide particles originating from the combustion of lubrication oil. The larger mode dominated PM mass while the smaller mode contributed significantly to PM number. When the engine was idling at berth, over 99% of the emitted PM mass was organic (volatile) and most likely also originated from lubrication oil. At engine loads above 25%, the majority of the emitted PM mass was BC, most likely originating from the diesel pilot fuel.

The PM measurements were placed in the context of diesel-only mode emissions from the same engine. The BC emissions were over an order of magnitude lower in LNG mode. As a consequence, the snow-and ice-albedo reductions due to BC deposition are predicted to be reduced by at least an order of magnitude in LNG mode. From a GWP perspective, BC emissions are negligible relative to co-emitted methane and CO_2 emissions in both LNG and diesel mode. The long-term (>100-year) GWP of LNG mode emissions was lower than the corresponding diesel mode emissions. The above conclusions do not account for idle emissions, which were over an order of magnitude higher in both cases; idling at low loads should be avoided. In addition, engine emissions may vary substantially between vessels, and emissions-control technology may substantially mitigate the negative impacts of some of the engine emissions.

Author contributions

SG conceived and coordinated the study and WM, PL, PK and SG initiated the study. WP, DS, JY, and PK performed the gaseous measurements. UT performed the TEM analysis. SR, DRC, PK, and WP supervised students. JCC performed the particulate measurements, analyzed and interpreted the data with contributions by WP and DS, and wrote the manuscript.

Declaration of competing interest

The authors declare that they have no known competing financial interests or personal relationships that could have appeared to influence the work reported in this paper.

Acknowledgements

The authors are very grateful to the vessel operators for their willingness to facilitate this study. We thank Brett Smith (NRC) for assistance with the measurements and logistics. Funding from Transport Canada and the United States Maritime Administration (MARAD) is gratefully acknowledged. Any conclusions or recommendations expressed in this paper are those of the authors and do not necessarily reflect the views of the vessel operator or the sponsoring agencies.

Appendix A. Supplementary data

Supplementary data to this article can be found online at https://doi.org/10.1016/j.atmosenv.2019.117030.

References

Alanen, J., Saukko, E., Lehtoranta, K., Murtonen, T., Timonen, H., Hillamo, R., Karjalainen, P., Kuuluvainen, H., Harra, J., Keskinen, J., Rönkkö, T., 2015. The formation and physical properties of the particle emissions from a natural gas engine. Fuel 162, 155–161. https://doi.org/10.1016/j.fuel.2015.09.003.

M. R. Allen, K. P. Shine, J. S. Fuglestvedt, R. J. Millar, M. Cain, D. J. Frame, A. H. Macey, A solution to the misrepresentations of CO2-equivalent emissions of short-lived climate pollutants under ambitious mitigation, npj Clim. Atmos. Sci. 1 (1). doi: 10.1038/s41612-018-0026-8.

Anderson, M., Salo, K., Fridell, E., 2015. Particle- and gaseous emissions from an LNG powered ship. Environ. Sci. Technol. 49 (20), 12568–12575. https://doi.org/10.1021/acs.est.5b02678.

Archer, D., Eby, M., Brovkin, V., Ridgwell, A., Cao, L., Mikolajewicz, U., Caldeira, K., Matsumoto, K., Munhoven, G., Montenegro, A., Tokos, K., 2009. Atmospheric lifetime of fossil fuel carbon dioxide. Annu. Rev. Earth Planet Sci. 37 (1), 117–134. https://doi.org/10.1146/annurev.earth.031208.100206.

Benbrahim-Tallaa, L., Baan, R.A., Grosse, Y., Lauby-Secretan, B., El Ghissassi, F., Bouvard, V., Guha, N., Loomis, D., Straif, K., 2012. Carcinogenicity of diesel-engine and gasoline-engine exhausts and some nitroarenes. Lancet Oncol. 13 (7), 663–664. https://doi.org/10.1016/S1470-2045(12)70280-2.

Bengtsson, S., Andersson, K., Fridell, E., 2011. A comparative life cycle assessment of marine fuels. Proc. Inst. Mech. Eng. M J. Eng. Marit. Environ. 225 (2), 97–110. https://doi.org/10.1177/1475090211402136.

Bengtsson, S., Fridell, E., Andersson, K., 2012. Environmental assessment of two pathways towards the use of biofuels in shipping. Energy Policy 44, 451–463. https://doi.org/10.1016/j.enpol.2012.02.030.

Bengtsson, S.K., Fridell, E., Andersson, K.E., 2013. Fuels for short sea shipping: a comparative assessment with focus on environmental impact. Proc. Inst. Mech. Eng. M J. Eng. Marit. Environ. 228 (1), 44–54. https://doi.org/10.1177/1475090213480349.

Bond, T.C., Bergstrom, R.W., 2006. Light absorption by carbonaceous particles: an investigative review. Aerosol Sci. Technol. 40 (1), 27–67. https://doi.org/10.1080/02786820500421521.

Bond, T.C., Sun, H., 2005. Can reducing black carbon emissions counteract global warming? Environ. Sci. Technol. 39 (16), 5921–5926. https://doi.org/10.1021/es0480421.

Bond, T.C., Doherty, S.J., Fahey, D.W., Forster, P.M., Berntsen, T., DeAngelo, B.J., Flanner, M.G., Ghan, S., Kärcher, B., Koch, D., Kinne, S., Kondo, Y., Quinn, P.K., Sarofim, M.C., Schultz, M.G., Schulz, M., Venkataraman, C., Zhang, H., Zhang, S., Bellouin, N., Guttikunda, S.K., Hopke, P.K., Jacobson, M.Z., Kaiser, J.W., Klimont, Z., Lohmann, U., Schwarz, J.P., Shindell, D., Storelvmo, T., Warren, S.G., Zender, C.S., 2013. Bounding the role of black carbon in the climate system: a scientific assessment. J. Geophys. Res. Atmos. 118, 5380–5552. https://doi.org/10.1002/jgrd.50171.

Boucher, O., Randall, D., Artaxo, P., Bretherton, C., Feingold, G., Forster, P., Kerminen, V., Kondo, Y., Liao, H., Lohmann, U., Rasch, P., Satheesh, S., Sherwood, S., Stevens, B., Zhang, X., 2013. Clouds and Aerosols. Cambridge University Press. http://www.ipcc.ch/report/ar5/wg1/.

Bullock, D.S., Olfert, J.S., 2014. Size, volatility, and effective density of particulate emissions from a homogeneous charge compression ignition engine using compressed natural gas. J. Aerosol Sci. 75, 1–8. https://doi.org/10.1016/j.jaerosci.2014.04.005.

Cavalli, F., Viana, M., Yttri, K.E., Genberg, J., Putaud, J.-P., 2010. Toward a standardised thermal-optical protocol for measuring atmospheric organic and elemental carbon: the EUSAAR protocol. Atmos. Meas. Tech. 3 (1), 79–89. https://doi.org/10.5194/amt-3-79-2010.

Coggon, M.M., Sorooshian, A., Wang, Z., Metcalf, A.R., Frossard, A.A., Lin, J.J., Craven, J.S., Nenes, A., Jonsson, H.H., Russell, L.M., Flagan, R.C., Seinfeld, J.H., 2012. Ship impacts on the marine atmosphere: insights into the contribution of shipping emissions to the properties of marine aerosol and clouds. Atmos. Chem. Phys. 12 (18), 8439–8458. https://doi.org/10.5194/acp-12-8439-2012.

J. C. Corbin, H. Czech, D. Massabo, F. Buatier de Mongeot, G. Jakobi, F. Liu, P. Lobo, C. Mennucci, A. A. Mensah, J. Orasche, S. M. Pieber, A. S. H. Prévôt, B. Stengel, L. L. Tay, M. Zanatta, R. Zimmermann, I. El Haddad, M. Gysel-Beer, Refractory, infrared-

absorbing carbon in ship exhaust from heavy fuel oil combustion, npj Atmos. Clim. Sci. (12). doi:10.1038/s41612-019-0069-5.
M. Gysel, M. Laborde, A. A. Mensah, J. C. Corbin, A. Keller, J. Kim, A. Petzold, B. Sierau, Technical note: the single particle soot photometer fails to reliably detect palas soot nanoparticles, Atmos. Meas. Tech. 5. doi:10.5194/amt-5-3099-2012.
Gysel, N.R., Welch, W.A., Johnson, K., Miller, W., Cocker, D.R., 2017. Detailed analysis of criteria and particle emissions from a very large crude carrier using a novel ECA fuel. Environ. Sci. Technol. 51 (3), 1868–1875. https://doi.org/10.1021/acs.est.6b02577.
Hajbabaei, M., Karavalakis, G., Johnson, K.C., Lee, L., Durbin, T.D., 2013. Impact of natural gas fuel composition on criteria, toxic, and particle emissions from transit buses equipped with lean burn and stoichiometric engines. Energy 62, 425–434. https://doi.org/10.1016/j.energy.2013.09.040.
Hallquist, Å.M., Jerksjö, M., Fallgren, H., Westerlund, J., Sjödin, Å., 2013. Particle and gaseous emissions from individual diesel and CNG buses. Atmos. Chem. Phys. 13 (10), 5337–5350. https://doi.org/10.5194/acp-13-5337-2013.
IPCC, 2007. Contribution of Working Group I to the Fourth Assessment Report of the Intergovernmental Panel on Climate Change. Cambridge University Press, United Kingdom and New York, NY, USA.
Jacob, D., 1999. Introduction to Atmospheric Chemistry. Princeton University Press, Princeton, NJ, USA.
Jayaratne, E.R., Meyer, N.K., Ristovski, Z.D., Morawska, L., 2011. Volatile properties of particles emitted by compressed natural gas and diesel buses during steady-state and transient driving modes. Environ. Sci. Technol. 46 (1), 196–203. https://doi.org/10.1021/es2026856.
Korakianitis, T., Namasivayam, A., Crookes, R., 2011. Natural-gas fueled spark-ignition (SI) and compression-ignition (CI) engine performance and emissions. Prog. Energy Combust. Sci. 37 (1), 89–112. https://doi.org/10.1016/j.pecs.2010.04.002.
Kulkarni, P., Baron, P.A., Willeke, K., 2011. Aerosol Measurement: Principles, Techniques, and Applications. John Wiley & Sons.
Lehtoranta, K., Aakko-Saksa, P., Murtonen, T., Vesala, H., Ntziachristos, L., Rönkkö, T., Karjalainen, P., Kuittinen, N., Timonen, H., 2019. Particulate mass and nonvolatile particle number emissions from marine engines using low-sulfur fuels, natural gas, or scrubbers. Environ. Sci. Technol. 53 (6), 3315–3322. https://doi.org/10.1021/acs.est.8b05555.
Li, J., Wu, B., Mao, G., 2015. Research on the performance and emission characteristics of the LNG-diesel marine engine. J. Nat. Gas Sci. Eng. 27, 945–954. https://doi.org/10.1016/j.jngse.2015.09.036.
Lipsky, E.M., Robinson, A.L., 2006. Effects of dilution on fine particle mass and partitioning of semivolatile organics in diesel exhaust and wood smoke. Environ. Sci. Technol. 40 (1), 155–162. https://doi.org/10.1021/es050319p.
Mayer, A.C., Ulrich, A., Czerwinski, J., Mooney, J.J., 2010. Metal-oxide particles in combustion engine exhaust. In: SAE Technical Paper Series, No. 2010-01-0792. SAE International. https://doi.org/10.4271/2010-01-0792.
McWhinney, R.D., Badali, K., Liggio, J., Li, S.-M., Abbatt, J.P., 2013. Filterable redox cycling activity: a comparison between diesel exhaust particles and secondary organic aerosol constituents. Environ. Sci. Technol. 47 (7), 3362–3369. https://doi.org/10.1021/es304676x.
Menon, S., Hansen, J., Nazarenko, L., Luo, Y., 2002. Climate effects of black carbon aerosols in China and India. Science 297 (5590), 2250–2253.
Miller, A., Frey, G., King, G., Sunderman, C., 2010. A handheld electrostatic precipitator for sampling airborne particles and nanoparticles. Aerosol Sci. Technol. 44 (6), 417–427. https://doi.org/10.1080/02786821003692063.
Moosmüller, H., Arnott, W.P., 2009. Particle optics in the Rayleigh regime. J. Air Waste Manag. Assoc. 59 (9), 1028–1031. https://doi.org/10.3155/1047-3289.59.9.1028.
Moosmüller, H., Chakrabarty, R., Arnott, W., 2009. Aerosol light absorption and its measurement: a review. J. Quant. Spectrosc. Radiat. Transfer 110 (11), 844–878. https://doi.org/10.1016/j.jqsrt.2009.02.035.
Nakayama, T., Suzuki, H., Kagamitani, S., Ikeda, Y., Uchiyama, A., Matsumi, Y., 2015. Characterization of a three wavelength photoacoustic soot spectrometer (PASS-3) and a photoacoustic extinctiometer (PAX). J. Meteorol. Soc. Jpn. Ser. II 93 (2), 285–308. https://doi.org/10.2151/jmsj.2015-016.
Northrop, W.F., Bohac, S.V., Chin, J.-Y., Assanis, D.N., 2011. Comparison of filter smoke number and elemental carbon mass from partially premixed low temperature combustion in a direct-injection diesel engine. J. Eng. Gas Turbines Power 133 (10), 102804. https://doi.org/10.1115/1.4002918.
Oeder, S., Kanashova, T., Sippula, O., Sapcariu, S.C., Streibel, T., Arteaga-Salas, J.M., Passig, J., Dilger, M., Paur, H.-R., Schlager, C., Mülhopt, S., Diabaté, S., Weiss, C., Stengel, B., Rabe, R., Harndorf, H., Torvela, T., Jokiniemi, J., Hirvonen, M.-R., Schmidt-Weber, C., Traidl-Hoffmann, C., BéruBé, K.A., Wlodarczyk, A.J., Prytherch, Z., Michalke, B., Krebs, T., Prévôt, A.S.H., Kelbg, M., Tiggesbäumker, J., Karg, E., Jakobi, G., Scholtes, S., Schnelle-Kreis, J., Lintelmann, J., Matuschek, G., Sklorz, M., Klingbeil, S., Orasche, J., Richthammer, P., Müller, L., Elsasser, M., Reda, A., Gröger, T., Weggler, B., Schwemer, T., Czech, H., Rüger, C.P., Abbaszade, G., Radischat, C., Hiller, K., Buters, J.T.M., Dittmar, G., Zimmermann, R., 2015. Particulate matter from both heavy fuel oil and diesel fuel shipping emissions show strong biological effects on human lung cells at realistic and comparable in vitro exposure conditions. PLoS One 10 (6), e0126536. https://doi.org/10.1371/journal.pone.0126536.
Onasch, T.B., Massoli, P., Kebabian, P.L., Hills, F.B., Bacon, F.W., Freedman, A., 2015. Single scattering albedo monitor for airborne particulates. Aerosol Sci. Technol. 49 (4), 267–279. https://doi.org/10.1080/02786826.2015.1022248.
Pallapies, D., Taeger, D., Bochmann, F., Morfeld, P., 2013. Comment: carcinogenicity of diesel-engine exhaust (de). Arch. Toxicol. 87 (3), 547–549. https://doi.org/10.1007/s00204-012-0955-7.
Pan, C.-J.G., Schmitz, D.A., Cho, A.K., Froines, J., Fukuto, J.M., 2004. Inherent redox properties of diesel exhaust particles: catalysis of the generation of reactive oxygen species by biological reductants. Toxicol. Sci. 81 (1), 225–232. https://doi.org/10.1093/toxsci/kfh199.
Papagiannakis, R., Hountalas, D., 2004. Combustion and exhaust emission characteristics of a dual fuel compression ignition engine operated with pilot diesel fuel and natural gas. Energy Convers. Manag. 45 (18–19), 2971–2987. https://doi.org/10.1016/j.enconman.2004.01.013.
Park, K., Cao, F., Kittelson, D.B., McMurry, P.H., 2003. Relationship between particle mass and mobility for diesel exhaust particles. Environ. Sci. Technol. 37 (3), 577–583. https://doi.org/10.1021/es025960v.
Petzold, A., Ogren, J., Fiebig, M., Laj, P., Li, S.-M., Baltensperger, U., Holzer-Popp, T., Kinne, S., Pappalardo, G., Sugimoto, N., Wehrli, C., Wiedensohler, A., Zhang, X.-Y., 2013. Recommendations for the interpretation of "black carbon" measurements. Atmos. Chem. Phys. 13 (16), 8365–8379. https://doi.org/10.5194/acp-13-8365-2013.
Pierrehumbert, R., 2014. Short-lived climate pollution. Annu. Rev. Earth Planet Sci. 42 (1), 341–379. https://doi.org/10.1146/annurev-earth-060313-054843.
Quinn, P.K., Stohl, A., Arnold, S., Baklanov, A., Berntsen, T., Christensen, J.H., Eckhardt, S., Flanner, M., Klimont, Z., Korsholm, Z., Kupiainen, K., Langner, J., Law, K.S., Monks, S., von Salzen, K., Sand, M., Schmale, J., Vestreng, V., AMAP Assessment, 2015. Black Carbon and Ozone as Arctic Climate Forcers, Arctic Monitoring and Assessment Programme (AMAP), 2015. http://www.amap.no/documents/doc/amap-assessment-2015-black-carbon-and-ozone-as-arctic-climate-forcers/1299.
Schindler, W., Haisch, C., Beck, H.A., Niessner, R., Jacob, E., Rothe, D., 2004. A photoacoustic sensor system for time resolved quantification of diesel soot emissions. In: SAE Technical Paper Series, SAE International. https://doi.org/10.4271/2004-01-0968.
Schmid, H., Laskus, L., Abraham, H.J., Baltensperger, U., Lavanchy, V., Bizjak, M., Burba, P., Cachier, H., Crow, D., Chow, J., Gnauk, T., AEven, A., ten Brink, H.M., Giesen, K.-P., Hitzenberger, R., Hueglin, C., Maenhaut, W., Pio, C., Carvalho, A., Putaud, J.-P., Toom-Sauntry, D., Puxbaum, H., 2001. Results of the "carbon conference" international aerosol carbon round robin test stage i. Atmos. Environ. 35 (12), 2111–2121. https://doi.org/10.1016/s1352-2310(00)00493-3.
Sharafian, A., Blomerus, P., Mérida, W., 2019. Natural gas as a ship fuel: assessment of greenhouse gas and air pollutant reduction potential. Energy Policy 131, 332–346. https://doi.org/10.1016/j.enpol.2019.05.015.
Skeie, R.B., Berntsen, T., Myhre, G., Pedersen, C.A., Ström, J., Gerland, S., Ogren, J.A., 2011. Black carbon in the atmosphere and snow, from pre-industrial times until present. Atmos. Chem. Phys. 11 (14), 6809–6836. https://doi.org/10.5194/acp-11-6809-2011.
Skiles, S.M., Flanner, M., Cook, J.M., Dumont, M., Painter, T.H., 2018. Radiative forcing by light-absorbing particles in snow. Nat. Clim. Chang. 8 (11), 964–971. https://doi.org/10.1038/s41558-018-0296-5.
Snelling, D.R., Smallwood, G.J., Liu, F., Gülder, Ömer L., Bachalo, W.D., 2005. A calibration-independent laser-induced incandescence technique for soot measurement by detecting absolute light intensity. Appl. Opt. 44 (31) https://doi.org/10.1364/ao.44.006773, 6773.
Sommer, D.E., Yeremi, M., Son, J., Corbin, J.C., Gagné, S., Lobo, P., Miller, J.W., Kirchen, P., 2019. Characterization and reduction of in-use CH4 emissions from a dual fuel marine engine using wavelength modulation spectroscopy. Environ. Sci. Technol. 53 (5), 2892–2899. https://doi.org/10.1021/acs.est.8b04244.
Sun, Y., Bochmann, F., Nold, A., Mattenklott, M., 2014. Diesel exhaust exposure and the risk of lung cancer–a review of the epidemiological evidence. Int. J. Environ. Res. Public Health 11 (2), 1312–1340. https://doi.org/10.3390/ijerph110201312.
Swanson, J., Kittelson, D., 2009. Factors influencing mass collected during 2007 diesel PM filter sampling. SAE Int. J. Fuels Lubr. 2 (1), 718–729. https://doi.org/10.4271/2009-01-1517.
Tartakovsky, L., Sheintuch, M., 2018. Fuel reforming in internal combustion engines. Prog. Energy Combust. Sci. 67, 88–114. https://doi.org/10.1016/j.pecs.2018.02.003.
Thomson, H., Corbett, J.J., Winebrake, J.J., 2015. Natural gas as a marine fuel. Energy Policy 87, 153–167. https://doi.org/10.1016/j.enpol.2015.08.027.
Tree, D.R., Svensson, K.I., 2007. Soot processes in compression ignition engines. Prog. Energy Combust. Sci. 33 (3), 272–309. https://doi.org/10.1016/j.pecs.2006.03.002.
Trivanovic, U., Corbin, J.C., Baldelli, A., Peng, W., Yang, J., Kirchen, P., Miller, J.W., Lobo, P., Gagné, S., Rogak, S.N., 2019. Size and morphology of soot produced by a dual-fuel marine engine. J. Aerosol Sci. 138 https://doi.org/10.1016/j.jaerosci.2019.105448.
Turrio-Baldassarri, L., Battistelli, C.L., Conti, L., Crebelli, R., Berardis, B.D., Iamiceli, A.L., Gambino, M., Iannaccone, S., 2006. Evaluation of emission toxicity of urban bus engines: compressed natural gas and comparison with liquid fuels. Sci. Total Environ. 355 (1–3), 64–77. https://doi.org/10.1016/j.scitotenv.2005.02.037.
von der Weiden, S.-L., Drewnick, F., Borrmann, S., 2009. Particle loss calculator – a new software tool for the assessment of the performance of aerosol inlet systems. Atmos. Meas. Tech. 2 (2), 479–494. https://doi.org/10.5194/amt-2-479-2009.
Wilson, M.D., Rocke, D.M., Durbin, B., Kahn, H.D., 2004. Detection limits and goodness-of-fit measures for the two-component model of chemical analytical error. Anal. Chim. Acta 509 (2), 197–208. https://doi.org/10.1016/j.aca.2003.12.047.

S1. Supplement to *Short-lived climate pollutant emissions from a liquid-natural-gas marine engine* by J. C. Corbin et al., Atmos. Env. 2019

This supplement contains:

- Details on the calculation of eBC by the AVL 415S.
- Additional information on the XRF measurements.
- A diagram of the instrumental layout during this study.
- Data on a test of the catalytic stripper efficiency for our 50% load samples,
- Additional load-dependent size distributions,
- other figures cited in the main text.

S1.1. AVL 415S calculation of eBC

According to the product manual, the AVL 415S smoke meter calculates eBC using the equation,

$$eBC(560\text{nm}) = \frac{5.32\text{F}e^{0.3062F}}{0.405} \tag{S1}$$

where F is the filter smoke number (FSN) and eBC(560nm) is equivalent black carbon at 560 nm in mg/m^3. We refer to this quantity as eBC because it fundamentally relies on a measurement of light attenuation (which is related to light absorption).

S1.2. Additional tables

Table S1 presents a summary of the test points analyzed in this study. Table S2 presents the X-ray fluorescence (XRF) measurements of the PM in either engine mode.

S1.3. Additional figures

Figures S1–S9 provide additional information and data, as described below. The original data are avaliable upon request.

Date	Fuel	Test point duration [min]	Test point index	Engine load	Filter sample taken
2018-04-11	LNG	40	0	50	1
2018-04-11	LNG	47	1	6	1
2018-04-11	LNG	77	2	50	1
2018-04-12	LNG	49	3	6	0
2018-04-12	LNG	58	4	75	1
2018-04-12	LNG	100	5	6	1
2018-04-12	LNG	38	6	90	1
2018-04-12	LNG	53	7	90	0
2018-04-13	LNG	45	8	31	1
2018-04-13	LNG	45	9	53	0
2018-04-13	LNG	4	10	60	0
2018-04-13	LNG	27	11	60	0
2018-04-13	LNG	36	12	30	0
2018-04-13	LNG	33	13	85	0
2018-04-15	Diesel	61	14	25	1
2018-04-15	Diesel	50	15	50	0
2018-04-15	Diesel	64	16	75	0
2018-04-15	Diesel	84	17	0	0

Table S1: Summary of the test points and their respective durations for each test analyzed in this study (except the cylinder-deactivation tests). The rightmost column is 1 when a filter was analyzed by TOA and 0 otherwise.

		Metal concentration [$\mu g\,cm^{-2}$]								
Sample	Filter ID	Mg	Si	P	Cl	Ca	Fe	Cu	Zn	Mo
MDL[a]		0.054	0.023	0.012	0.011	0.014	0.020	0.006	0.006	0.008
LNG	T171077	0.048	0.023	0.008	0.007	0.018	0.001	0.013	0.010	0.004
LNG	T171079	0.040	0.025	0.010	0.008	0.053	0.021	0.003	0.007	0.006
LNG	T180015	0.025	0.037	0.003	0.008	0.028	0.001	0.002	0.005	0.004
LNG	T180011	0.048	0.013	0.008	0.008	0.036	0.009	0.003	0.010	0.004
LNG	T180058	0.031	0.020	0.009	0.007	0.044	0.004	0.003	0.011	0.003
LNG	T180095	0.056	0.021	0.010	0.007	0.039	0.001	0.004	0.008	0.002
LNG	T180062	0.031	0.014	0.007	0.006	0.037	0.005	0.001	0.007	0.004
Diesel	T180080	0.042	0.019	0.032	0.011	0.135	0.002	0.002	0.027	0.022
Diesel	T180075	0.030	0.007	0.043	0.008	0.158	ND	ND	0.031	0.026
Diesel	T180069	0.028	0.009	0.065	0.010	0.234	0.004	0.002	0.050	0.043
Diesel	T180070	0.018	0.007	0.093	0.012	0.363	0.003	0.003	0.068	0.063
Diesel	T180076	0.028	0.010	0.095	0.013	0.348	0.003	0.001	0.066	0.060
Diesel	T180077	0.029	0.014	0.119	0.017	0.439	0.009	0.001	0.077	0.070
Mean LNG		0.040	0.022	0.008	0.007	0.036	0.006	0.004	0.008	0.004
Mean Diesel		0.029	0.011	0.074	0.012	0.279	0.004	0.002	0.053	0.047
SD LNG		0.011	0.008	0.003	0.001	0.011	0.007	0.004	0.002	0.001
SD diesel		0.008	0.005	0.034	0.003	0.122	0.003	0.001	0.021	0.020
Ratio LNG/Diesel		1.37	2.01	0.10	0.60	0.13	1.45	2.27	0.15	0.08
SD of Ratio		0.81	1.51	0.08	0.32	0.09	2.12	2.80	0.10	0.06
Ratio where RSD $< 50\%$						0.13			0.15	

Table S2: XRF results for the metal content of PM from LNG mode and diesel mode. The lower seven rows show the mean concentrations and ratio of mean concentrations for each element. [a]Data are only shown where the measured concentrations exceeded the method detection limit at least once. This condition applies to the following elements: Na, Al, S, K, Ti, V, Cr, Mn, Co, Ni, Ga, Ge, As, Se, Br, Rb, Sr, Y, Zr, Nb, Rh, Pd, Ag, Cd, In, Sn, Sb, Te, Cs, Ba, La, Ce, Nd, Sm, Gd, Pt, Au, Tl, Pb, Bi, U.

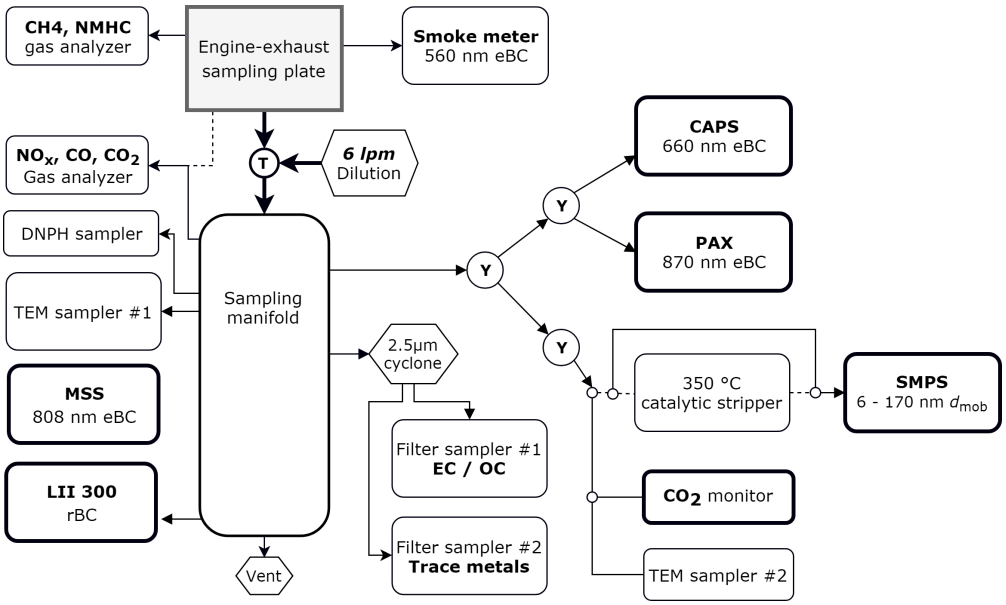

Figure S1: Experimental configuration. Thicker lines denote real-time instruments. Dashed lines indicate temporary connections as described in the text. The letters Y and T describe the wye and tee flow splitter or mixer used.

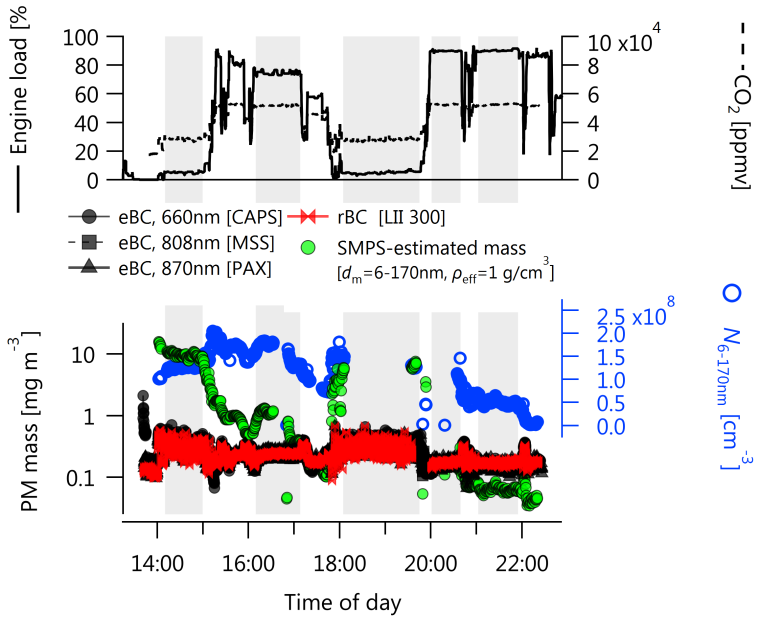

Figure S2: Similar to Figure 1 but zoomed out to show the entire day of measurements. The gaps in th data around 19:00 reflect a period where sampling was briefly interrupted. Grey-shaded regions illustrate some of the periods of stable engine conditions which were averaged in Figure S8.

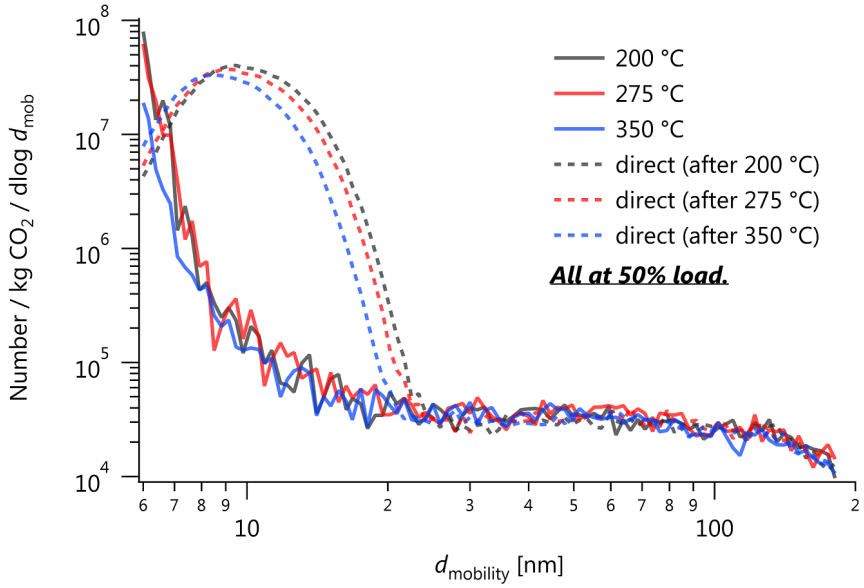

Figure S3: Mobility-size distributions of LNG exhaust as a function of catalytic-stripper temperature. The independence of the result on temperature indicates that the smallest particle mode is not an artifact of the incomplete removal of volatiles. This result is consistent with those of [19] who found that the majority of natural-gas-engine PM volatilized below 360 K. These tests were performed at 50 % engine load.

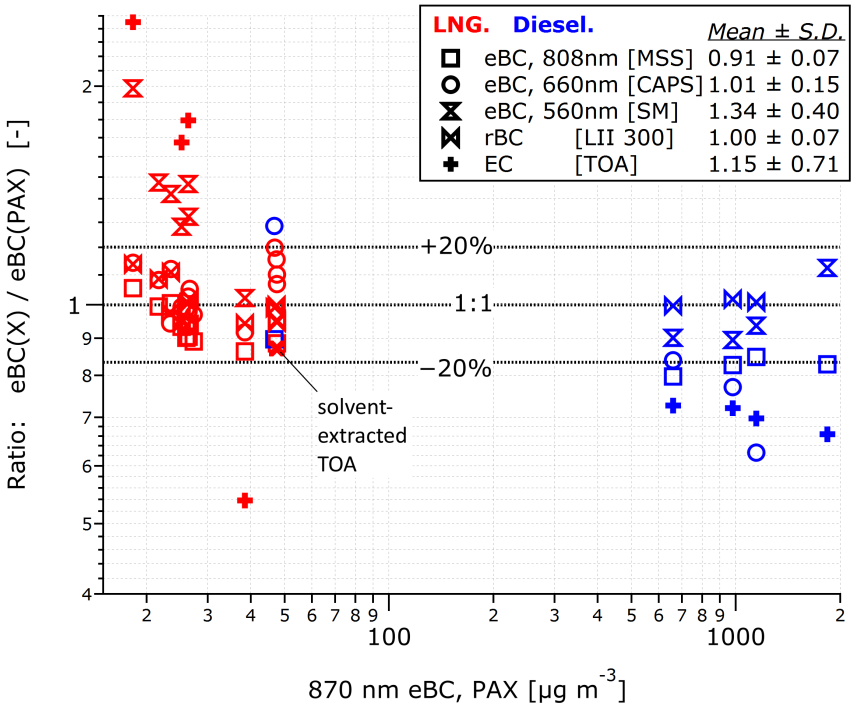

Figure S4: Ratio of measured BC concentrations to an arbitrary reference instrument (PAX) as a function of mass concentration and fuel. Red and blue symbols indicate LNG and diesel respectively. The PAX was selected as the reference instrument in this comparison because it was calibrated on-site and operated on the principle of light-absorption (eBC) measurement, in common with most other instruments. (Although the CAPS was also calibrated on-site, the diesel-mode eBC concentrations are outside of its specified range of operation; as shown by the negative bias of the corresponding data points.) Some data were not available for the highest measured diesel concentration. The dotted horizontal lines show the 1:1 line along with a 20% uncertainty.

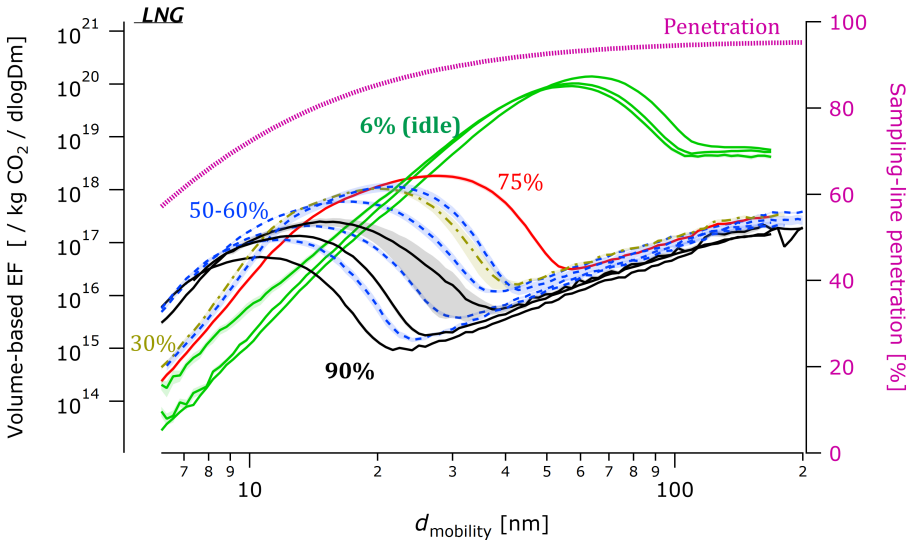

Figure S5: Mean volume-weighted mobility-size distributions for LNG combustion as a function of engine load. Different engine loads are identified by label, colour, and line dash type. Shading shows standard error of the mean. Also shown on the right axis is the size-resolved sampling line penetration calculated for our sampling system using the tool published by von der Weiden et al.[43].

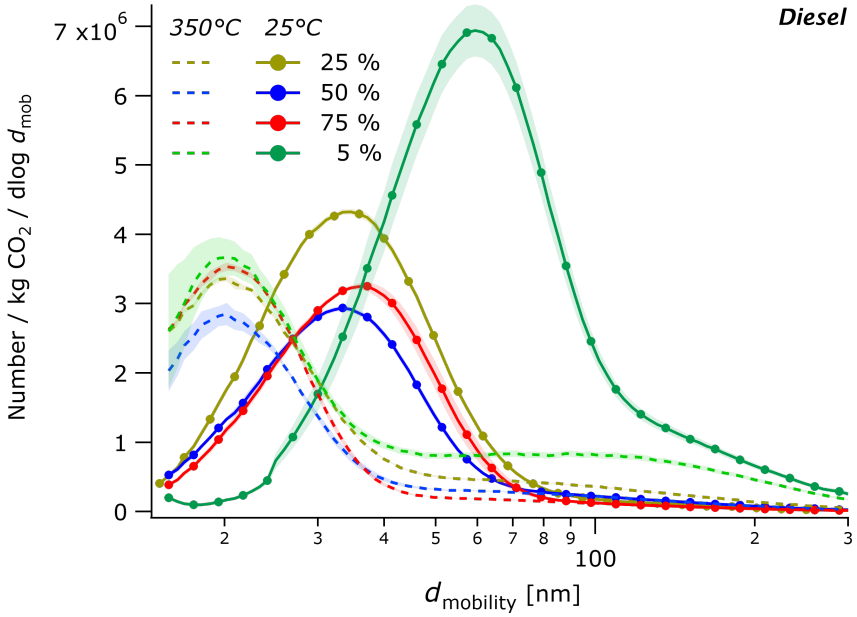

Figure S6: Mean mobility-size number distributions for diesel combustion as a function of engine load. Solid lines show sixfold-diluted samples, dashed lines show samples denuded at 623 K. Shading shows standard error of the mean.

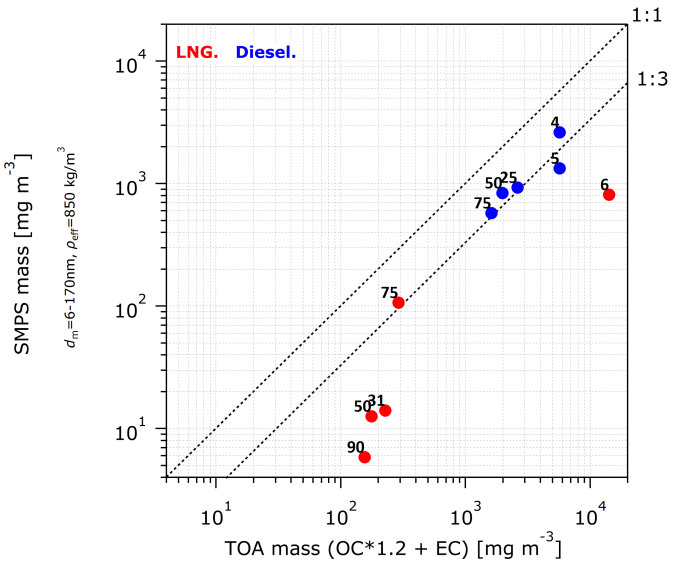

Figure S7: SMPS-estimated particulate mass versus TOA-estimated mass. The SMPS-estimated mass is the integrated volume of measured particles, converted to mass using an effective density of 850 kg m^{-3} as discussed in the main text. The TOA-estimated mass is the sum of OC and EC, with OC multiplied by a factor of 1.2 to account for the fact that total organic mass includes not just the carbon measured by TOA but also oxygen [61]. The SMPS is known to underestimate total mass as not all particle volume was measured (Figure S5); TOA is therefore considered the more reliable measurement. Colours indicate fuel composition; numbers indicate engine load.

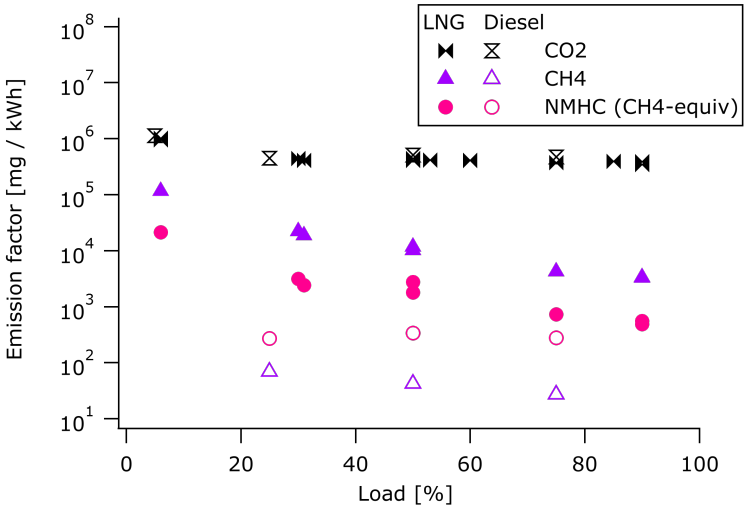

Figure S8: Gaseous emission factors versus load.

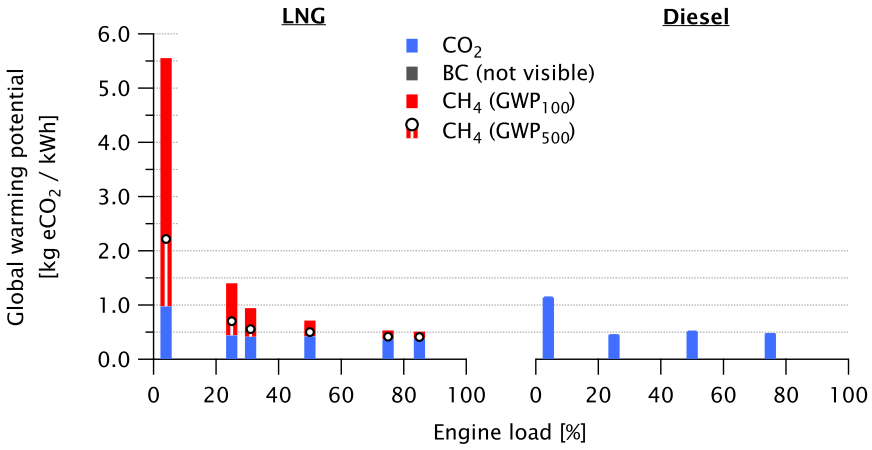

Figure S9: 100-year global warming potentials ($GWP_1 00$) for methane, CO2, and BC for this engine when operating in LNG or diesel mode. Note that these are considered worst-case GWPs as engine tuning may be able to reduce methane emissions. The vessel operator has used shore power rather than NG combustion when idling at shore as a result of this study, and therefore spends little time operating below 50% load. White circles show the change in GWP when using the GWP_{500} instead of the GWP_{100}. For the GWP_{25}, the methane GWP increases 7.6-fold. Note that black carbon climate effects are fundamentally different to methane and CO_2 warming effects, since black carbon continues to warm the climate after deposition onto highalbedo surfaces, as discussed in the main text. Note also that uncombusted methane is fundamentally different to CO_2 emissions, as it may be reduced by emissions-control technologies whereas CO_2 emissions may not. We also note that the climate impacts of NG-mode operation must be considered holistically, as emissions from production, supply, and bunkering are currently substantial [62].

SI References

[61] B. J. Turpin, H.-J. Lim, Species contributions to PM2.5 mass concentrations: Revisiting common assumptions for estimating organic mass, Aerosol Sci. Technol. 35 (1) (2001) 602–610. doi:10.1080/02786820119445.

[62] R. A. Alvarez, D. Zavala-Araiza, D. R. Lyon, D. T. Allen, Z. R. Barkley, A. R. Brandt, K. J. Davis, S. C. Herndon, D. J. Jacob, A. Karion, E. A. Kort, B. K. Lamb, T. Lauvaux, J. D. Maasakkers, A. J. Marchese, M. Omara, S. W. Pacala, J. Peischl, A. L. Robinson, P. B. Shepson, C. Sweeney, A. Townsend-Small, S. C. Wofsy, S. P. Hamburg, Assessment of methane emissions from the u.s. oil and gas supply chain, Science (2018) 186–188. doi:10.1126/science.aar7204.